JOURNAL OF GEOPHYSICAL RESEARCH, VOL. 113, B10311, doi:10.1029/2007JB005556, 2008

Observations and interpretation of fundamental mode Rayleigh wavefields recorded by the Transportable Array (USArray)

Fred F. Pollitz[1]

Received 17 December 2007; revised 8 May 2008; accepted 25 June 2008; published 16 October 2008.

[1] Broadband recordings of the dense Transportable Array (TA) in the western United States provide unparalleled detailed images of long-period seismic surface wavefields. With 400 stations spanning most of the western United States, wavefronts of fundamental mode Rayleigh waves may be visualized coherently across the array at periods $\gtrsim$40 s. In order to constrain the Rayleigh wave phase velocity structure in the western United States, I assemble a data set of vertical component seismograms from 53 teleseismic events recorded by the TA from April 2006 to October 2007. Complex amplitude spectra from these recordings at periods 27–100 s are interpreted using the multiplane wave tomographic method of Friederich and Wielandt (1995) and Pollitz (1999). This analysis yields detailed surface wave phase velocity and three-dimensional shear wave velocity patterns across the North American plate boundary zone, elucidating the active processes in the highly heterogeneous western U.S. upper mantle.

Citation: Pollitz, F. F. (2008), Observations and interpretation of fundamental mode Rayleigh wavefields recorded by the Transportable Array (USArray), *J. Geophys. Res.*, *113*, B10311, doi:10.1029/2007JB005556.

1. Introduction

[2] In regional seismic tomography, imaging capability has been typically limited by the distribution of receivers on Earth's surface. This situation changed dramatically with the advent of the USArray component of Earthscope: "a continental-scale seismic observatory designed to provide a foundation for integrated studies of continental lithosphere and deep Earth structure over a wide range of scales" (http://www.earthscope.org/index.php/es_obs/usarray_obs). One of its components is the Transportable Array (TA), which comprises 400 broadband stations (Figure 1) and covers an area $\sim$2000 $\times$ 1400 km^2 with a station spacing of about 70 km. This network is ideal for visualizing long-period seismic surface wavefields as well as laterally heterogeneous wave speed structure, addressing the crust and upper mantle structure beneath the tectonically diverse western United States (Figure 2). Since surface waves propagate essentially horizontally, they sample all portions of the array area and thus carry enormous imaging capability for the waveguide in which they propagate, e.g., the crust and upper mantle to a depth that scales with the horizontal wavelength.

[3] In this study, I focus on the fundamental mode Rayleigh waves at periods of 27–100 s, which are well recorded from numerous teleseismic events. In order to characterize lateral variations in phase velocity, I measure complex spectral amplitudes generated by large teleseismic events and interpret them in terms of the joint effects of incident wavefield complexity and phase velocity distribution over a large area spanning the TA (shaded area in Figure 1). The use of scattering theory allows the estimation of phase velocity at lateral scales of the order of one wavelength (100 to 400 km at the considered period range). This and the use of a dense seismic array allow estimation of detailed phase velocity distributions with good resolution. The phase velocity maps are used to infer shear wave velocity down to $\sim$200 km depth. In sections 2–5, I present the observations of surface wavefields, the method of interpretation, and the resulting seismic structure. I then discuss notable elements of the seismic structure of various tectonic terranes in the western United States (Figure 2).

2. Data Set

[4] I assemble a composite set of seismograms consisting of 16585 vertical component seismograms from up to 425 broadband stations of the Transportable Array, using 53 shallow focus teleseismic events of magnitude $\geq$6.3 recorded during the period April 2006 to October 2007. The portions of the seismograms corresponding to a group velocity window from 2.9 to 4.3 km/s are isolated, and complex spectral amplitudes measured using a multiple taper method [*Pollitz*, 1999]. Spectrograms are used to identify the Rayleigh wave dispersion and determine the frequency-dependent group velocity at which complex spectral amplitudes are estimated. Examples are shown in Figure 3. Following *Pollitz* [1999], at fixed angular frequency $\omega = 2\pi f$ and a given site $\mathbf{r}_i$, complex spectral amplitudes $\tilde{\Phi}(\omega; \mathbf{r}_i)$ are estimated by means of isolating the fundamental mode with a Slepian eigentaper $w(t)$ designed to maximize the signal at a target group arrival time and minimize spectral leakage. The target group arrival time is $t_{\rm group} = \Delta/U$, where Δ is the source-receiver distance and U is group velocity.

[1]U.S. Geological Survey, Menlo Park, California, USA.

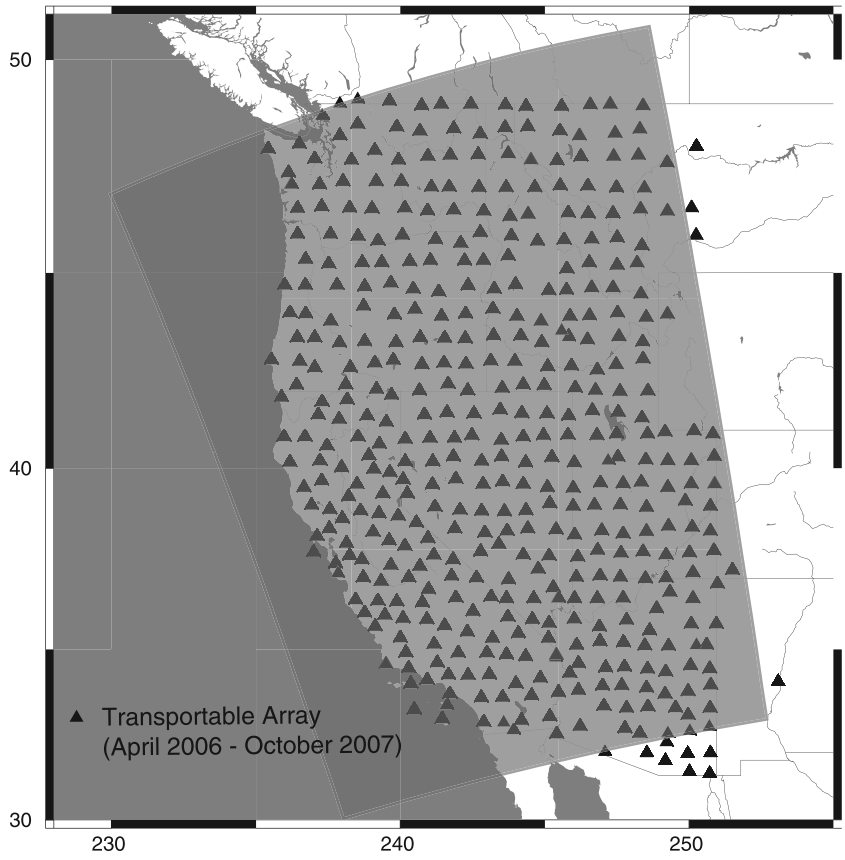

Figure 1. Distribution of broadband stations of the Transportable Array (TA) used in this study.

[5] At angular frequency ω define the Fourier transform of a function $f(t)$ as

$$F[f(t)](\omega) = \int_0^\infty f(t)\exp(-i\omega t)dt \tag{1}$$

Let $u(t)$ be the vertical component time series at $\mathbf{r}$, and define $\Phi(\omega;\mathbf{r}) = \frac{1}{U}F[u](\omega)$, i.e., the Rayleigh wave potential scaled by the vertical eigenfunction of the fundamental mode. Then the observed mode spectrum is

$$\tilde{\Phi}(\omega;\mathbf{r}) = \frac{1}{U}F[uw](\omega) = \frac{1}{2\pi}[\Phi^* W](\omega) \tag{2}$$

where asterisk is the convolution operator and $W(\omega) = F[w](\omega)$. Because of the dependence on t_{group}, the taper $w(t)$ and hence $\tilde{\Phi}$ are a function of U. The taper is constructed using a linear combination of the ten highest 6-π prolate Slepian tapers [*Park et al.*, 1987], each of which has an associated eigenvalue near unity and hence is highly bandlimited. This implies that the mode spectrum in equation (2) has little spectral leakage beyond angular frequency $\pm 12\pi/T$ about target frequency ω, where T is the length of the windowed portion of the seismogram used to isolate the surface waves; the limits of this window are defined by group velocities of 4.6 km/s and 2.6 km/s. An example of $w(t)$ is shown as a red curve in the MON seismogram of Figure 3. If T is $\sim$1000 s, then this half width is about 0.006 Hz. With this extended time window, high resolution in frequency is gained at the expense of reduced resolution in time. Temporal sidelobes of $w(t)$ have an amplitude up to 25% of $w(t_{\text{group}})$ and may sample other wave types. The time span T used to construct the optimal taper generally contains not only the direct fundamental mode arrival but also higher modes and later fundamental mode arrivals which may arise from multipathing (which may be viewed as surface waves associated with a wide outer Fresnel zone [e.g., *Zhou et al.*, 2004]). The use of shallow seismic sources and the selection criteria are designed to mitigate these noise sources. In addition, signal potentially contributed by multipathing is handled to first order by the theoretical modeling which accounts for the shape of the taper in constructing the sensitivity kernels (section 4.3).

[6] Using trial values of U from 2.9 to 4.3 km/s, $\tilde{\Phi}$ of the fundamental mode is taken at that group velocity $U = \hat{U}(f)$ for which $|\tilde{\Phi}|$ is maximized (asterisks in the spectrograms of Figure 3). A smooth polynomial fit to the dispersion curve $\bar{U}(f)$ is fit to the set of $\hat{U}(f)$ (curves in Figure 3). For a given event, a "summary" group velocity curve is defined as the average of the $\bar{U}(f)$ curves obtained for individual recordings of that event.

[7] Following *Pollitz* [1999], quality criteria are applied to edit the set $\{\tilde{\Phi}(\omega;\mathbf{r}_i)\}$. For a given seismogram and target frequency, these are based on the consistency of the records's $\bar{U}(f)$ with the event's summary group velocity curve, as well as the variance of the record's $\hat{U}(f) - \bar{U}(f)$ within a range of f about the target frequency. These criteria ensure that the same seismic phase is consistently identified

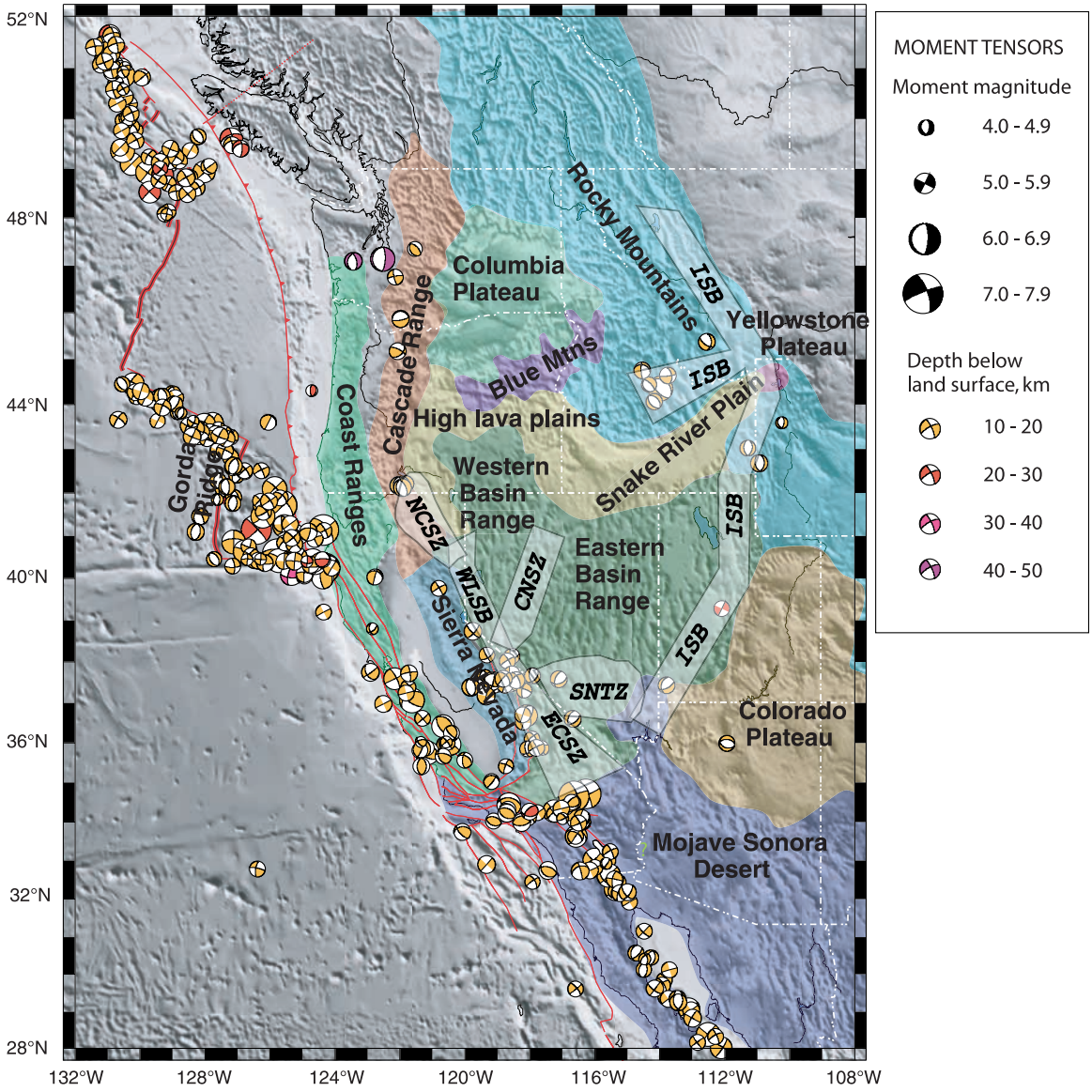

Figure 2. Tectonic map of the western United States with selected faults and focal mechanisms of earthquakes from 1976 to 2006 from the Harvard centroid moment tensor catalog. Seismic belts are based on the work by *Smith* [1978], *Stewart* [1988], *Dokka and Travis* [1990], and *Rogers et al.* [1991]. ISB, Intermountain Seismic Belt; ECSZ, Eastern California Shear Zone; CNSZ, Central Nevada Seismic Zone; WLSB, Walker Lane Seismic Belt; NCSZ, Northern California Shear Zone; SNTZ, Southern Nevada Transverse Zone.

from record to record and that the fundamental mode Rayleigh wave is of sufficiently high amplitude (e.g., above the noise level) and isolated from higher modes. At a given frequency, sources for which less than 60% of available measurements are retained are eliminated. As a result of applying the quality criteria, the set of acceptable sources varies according to frequency, and the set of seismic stations that yield acceptable observations varies according to the source and frequency.

3. Observed Wavefield Amplitude and Phase

[8] Wavefield amplitude A and phase ψ are defined in terms of the tapered full potentials as $A = |\tilde{\Phi}|$ and $\psi = \arg\tilde{\Phi} =$

Figure 3. Vertical component seismograms and associated spectrograms from four Transportable Array receivers (inset) which recorded the 31 January 2007 event of magnitude 6.5 (event 3 in the Figure 12 inset). Dashed lines delineate the time window defined by group velocities of 2.9 and 4.3 km/s. The red curve over the MONP seismogram shows the taper used to measure spectral amplitude of the 100 s Rayleigh wave. For a given spectrogram, asterisks indicate the group velocity $U(f)$ at which spectral amplitude at frequency f is maximum, and the superimposed curves are a cubic polynomial fit to $U(f)$.

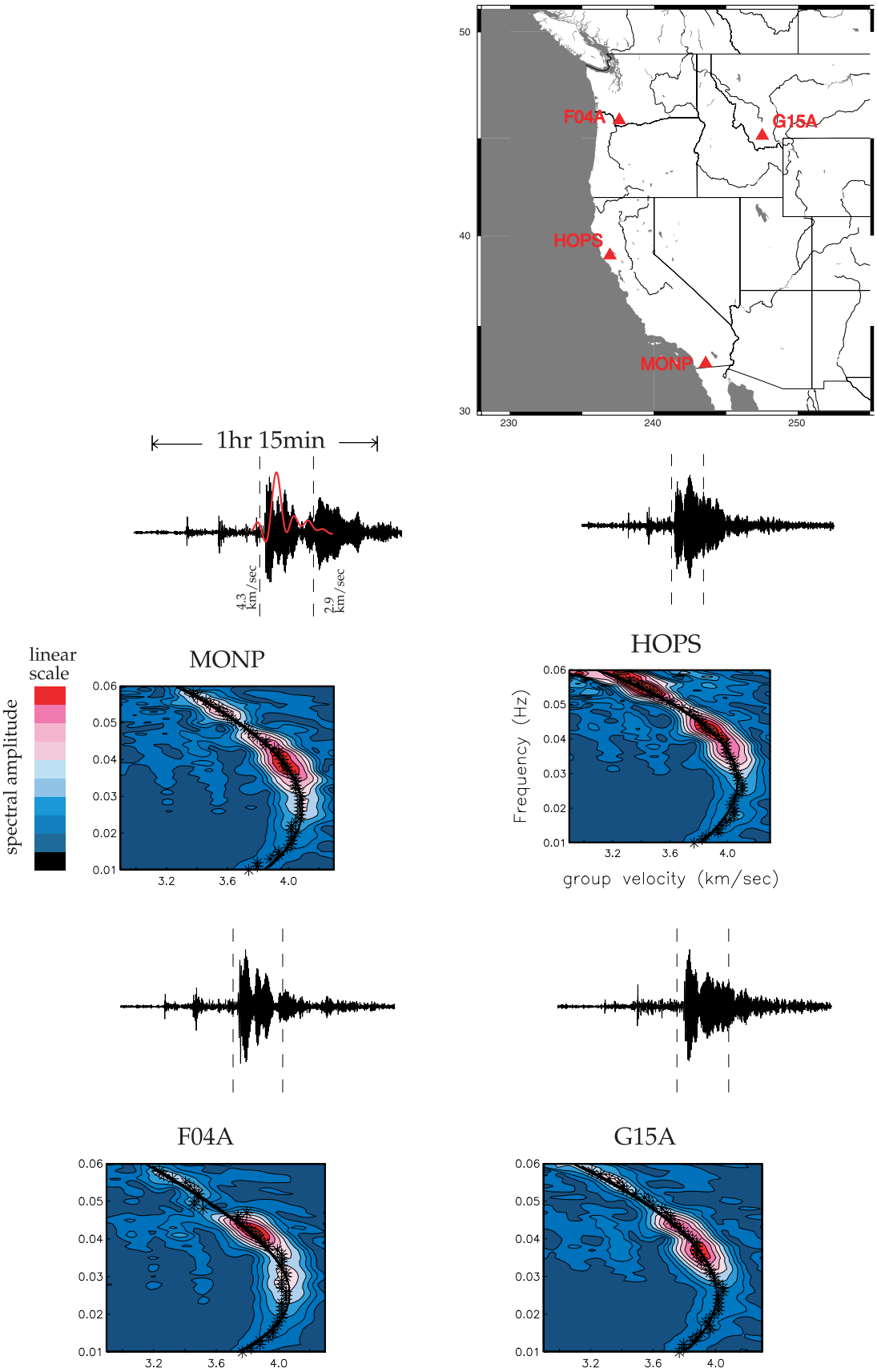
F04A
G15A
HOPS
MONP
50
40
30
230
240
250
1hr 15min
4.3 km/sec
2.9 km/sec
linear scale
spectral amplitude
MONP
HOPS
Frequency (Hz)
group velocity (km/sec)
F04A
G15A
0.06
0.05
0.04
0.03
0.02
0.01
3.2
3.6
4.0

Figure 3

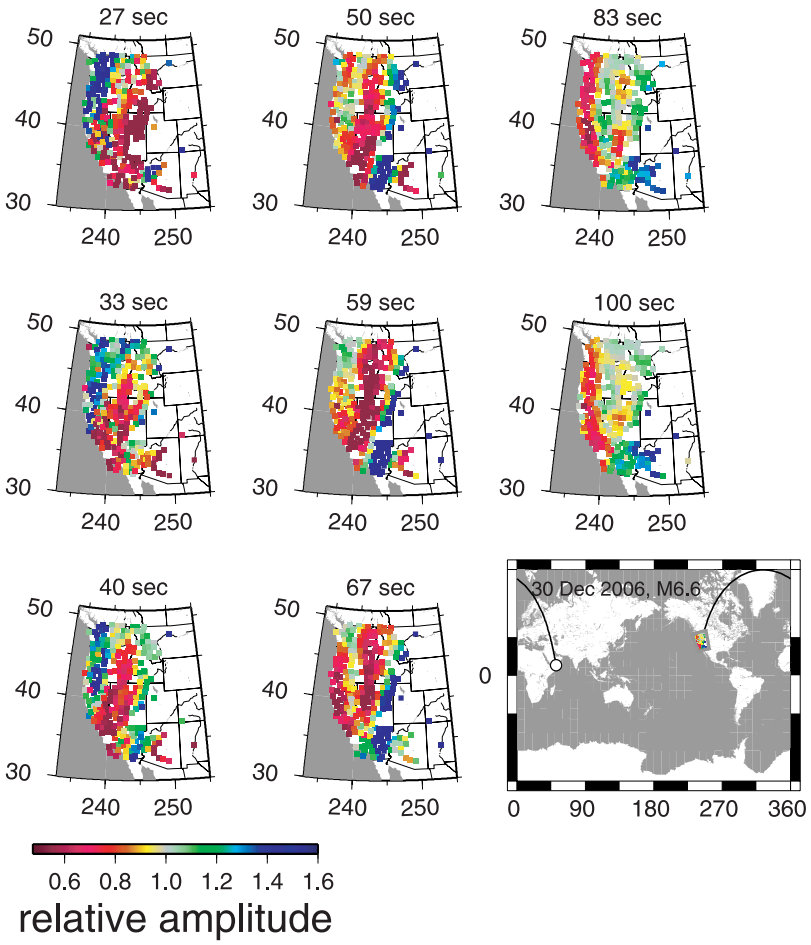

Figure 4. Relative amplitude of fundamental mode Rayleigh waves measured at Transportable Array sites at indicated periods for example event 1.

$\tan^{-1}(\mathrm{Im}\,\tilde{\Phi}/\mathrm{Re}\tilde{\Phi})$. Figures 4–7 show the observed wavefield amplitudes for four example events at periods of 27–100 s. For any event at a given period, the amplitude pattern is remarkably coherent and exhibits minor variation along the wave propagation direction (e.g., toward the northeast for event 3). At all periods, the amplitude pattern varies spatially at length scales $\gtrsim$200 km, yet for a given event the amplitude patterns are often not well correlated from period to period. A given region may record relatively low amplitudes for one event (e.g., northern California for event 2) but relatively high amplitudes for another event (e.g., northern California for event 4). Taken together, these features suggest that (1) the observed wavefield amplitude is shaped primarily by scattering from structure along the long teleseismic propagation path (through the Pacific Basin for events 2–4), (2) remote scattering effects are strongly frequency-dependent, and (3) at a given period, most of the lateral variation in amplitude is inherited from the teleseismic propagation path. The different amplitude patterns exhibited by events 2 and 4 on a period-by-period basis are particularly remarkable since the teleseismic propagation path is nearly identical for the two events. This suggests that the additional propagation path of event 4, about $\sim$15° geocentric degrees before it overlaps with the path of event 2, irrevocably shapes its character for the succeeding $\sim$60° of its propagation through the Pacific Basin. The difference in amplitude pattern may also arise from the greater width of the Fresnel zone for event 4 compared with event 2 because of the greater propagation distance [e.g., *Zhou et al.*, 2004]. In addition, amplitude variations along the wave propagation direction are witnessed in numerous instances (e.g., from coastal California to the Nevada border at most periods for event 3), indicating that scattering from aspherical structure within the continental western United States also contributes to observed amplitudes.

[9] Corresponding phase for the four example events is depicted in Figures 8–11 by cos ψ. At periods $\gtrsim$ 40 s, fronts of constant phase are remarkably coherent across the entire array, and they illustrate the increase in wavelength with period as well as wavefront distortion arising from interaction with seismic structure. Given the substantial lateral variability in amplitude, these apparently simple phase patterns likely contain laterally variable signal inherited from the teleseismic propagation path [*Wielandt*, 1993] as well as local structure. This highlights the need to describe the incident teleseismic wavefield with more than one plane wave [*Wielandt*, 1993; *Friederich and Wielandt*, 1995; *Pollitz*, 1999; *Yang and Forsyth*, 2006].

[10] The dependence of amplitude on period and its strong lateral variability (Figures 4–7) suggests that it depends on structure along the teleseismic propagation path in a highly nonlinear fashion. This behavior is also sug-

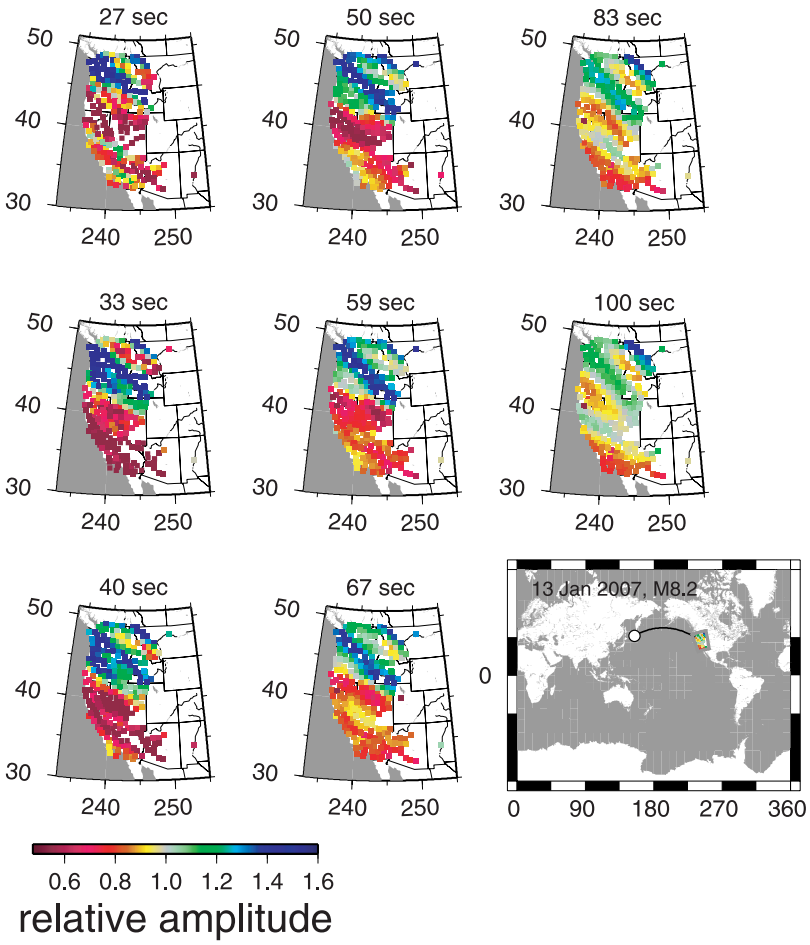

Figure 5. Relative amplitude of fundamental mode Rayleigh waves measured at Transportable Array sites at indicated periods for example event 2.

gested by theoretical considerations and numerical simulations [e.g., *Friederich et al.*, 1994; *Spetzler and Snieder*, 2001; *Hung et al.*, 2001; *Baig and Dahlen*, 2004]. *Hung et al.* [2001] note that for 3D waves (i.e., body waves), healing of phase is efficacious because the sensitivity kernel is identically zero on the geometrical raypath, and the width of the Fresnel zone affecting a receiver downstream from the structural anomaly increases with source-receiver distance; corresponding healing effects on amplitude may be diminished because its sensitivity is maximum on the geometrical raypath. For 2-D waves (i.e., surface waves), the situation is somewhat different because the phase sensitivity kernel is not zero on the direct raypath (section 4.3) [*Zhou et al.*, 2004], resulting in lessened wavefront healing in the 2-D case [*Nolet and Dahlen*, 2000]. However, the phase sensitivity kernel has a local minimum on the direct raypath while the amplitude sensitivity kernel has a local maximum on the direct raypath, so that diminished amplitude healing might be expected in the 2-D case. This issue warrants further numerical investigation.

[11] Local phase velocity c is given by $c = \lambda/T$, where T is period and λ is wavelength, which may be estimated visually from Figures 8–11 as the local distance to the next wave crest or trough. Wavefront phase varies to first order as $\psi \approx -(2\pi/cT)\Delta$, where Δ is distance from the source. Thus fronts of constant phase are expected to be offset toward the forward propagation direction upon passage through high-velocity structure. The wavefronts at latitude $\lesssim 37°$N for event 1, for example, directly suggest relatively high-velocity structure in the eastern part of the study area (i.e., east of Great Salt Lake). Similarly, the wavefronts for events 2 and 4 become increasingly convex with increasing propagation distance (toward the southeast) at all periods, directly suggesting relatively low-velocity structure in the Great Basin.

[12] Figures S1 and S2 in the auxiliary material[1] show additional examples of observed wavefield amplitude and phase, respectively, at different periods for a magnitude 6.3 event in the southwest Pacific in September 2007, when the TA had reached nearly its maximum aperture. As in the previous examples, the amplitude patterns are generally variable from period to period, but the wavefronts are remarkably coherent given the 10000 km propagation distance.

4. Determination of Phase Velocity Structure

[13] I interpret the set of measured complex spectral amplitudes with the method of joint estimation of incident wavefields and phase velocity structure as introduced by

[1]Auxiliary materials are available in the HTML. doi:10.1029/2007JB005556.

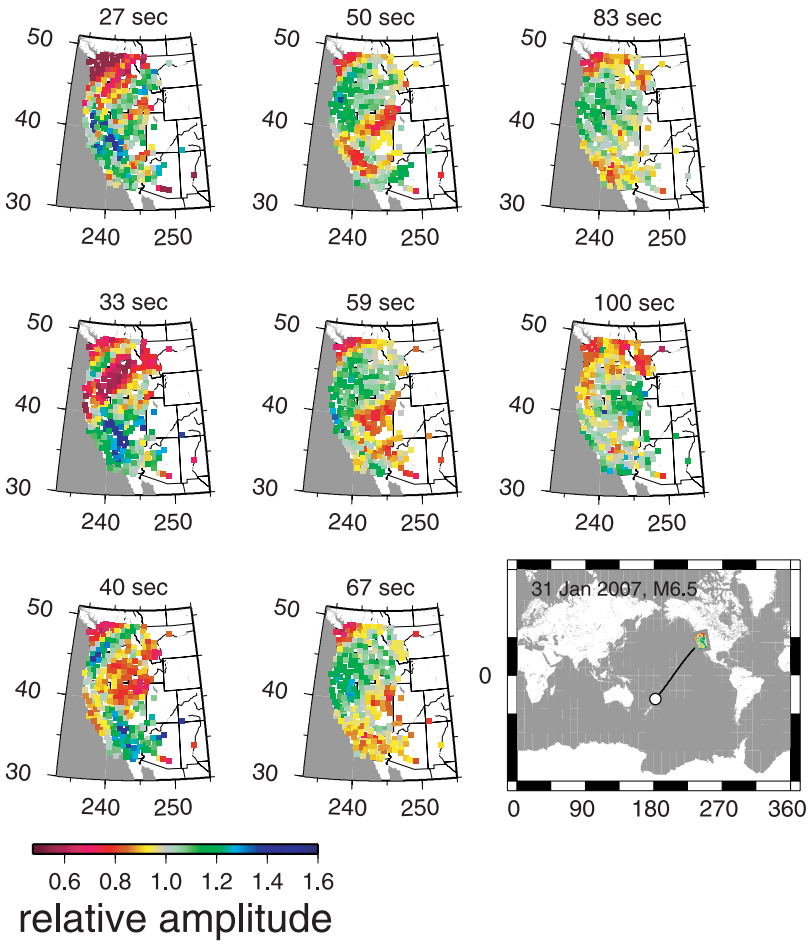

Figure 6. Relative amplitude of fundamental mode Rayleigh waves measured at Transportable Array sites at indicated periods for example event 3.

Friederich and Wielandt [1995] and modified by *Pollitz* [1999].

4.1. Helmholz Equation for Surface Wave Potential

[14] We work in a $r - \theta - \phi$ spherical coordinate system, using $\mathbf{r}$ to represent colatitude θ and longitude ϕ. A spherical membrane (unit sphere) is defined as the spherical shell $r = 1$. Define a portion of the unit sphere Ω that encompasses the array of receivers. At angular frequency $\omega = 2\pi/T$, we seek to find the Rayleigh wave potential $\Phi(\omega; \mathbf{r})$ which satisfies the Helmholz equation on a spherical membrane subject to laterally heterogeneous phase velocity $c(\omega; \mathbf{r})$:

$$c^2\Delta\Phi + \omega^2\Phi = 0 \tag{3}$$

The solution to equation (3) is given by the integral equation

$$\Phi(\omega;\mathbf{r}) = \Phi_0(\omega;\mathbf{r}) + 2k_0^2\int_{\mathbf{r}'\epsilon\Omega}\Phi(\omega;\mathbf{r}')\frac{\delta c(\omega;\mathbf{r}')}{c_0(\omega)}G(k_0;\mathbf{r},\mathbf{r}')d^2\mathbf{r}' \tag{4}$$

where $c_0(\omega)$ is phase velocity on a laterally homogeneous model; $k_0 = \omega/c_0(\omega)$, $\delta c(\omega; \mathbf{r}) = c(\omega; \mathbf{r}) - c_0(\omega)$; G is the response to a unit point scatterer at $\mathbf{r}'$ [e.g., *Dahlen* 1980]

$$c_0^2\Delta G(k_0;\mathbf{r},\mathbf{r}') + \omega^2 G(k_0;\mathbf{r},\mathbf{r}') = \delta(\mathbf{r},\mathbf{r}') \tag{5}$$

where $\delta(\mathbf{r}, \mathbf{r}')$ is a delta function that integrates to unity on an arbitrarily small area $d^2\mathbf{r}'$ around $\mathbf{r}$; and the *incident wavefield* Φ_0 satisfies

$$c_0^2\Delta\Phi_0 + \omega^2\Phi_0 = 0 \tag{6}$$

The incident wavefield Φ_0 includes in principle the effects of scattering from structure outside the study area ($\mathbf{r} \notin \Omega$).

[15] From equations (2) and (4), if the taper $w(t)$ used to estimate the surface wave spectra is highly bandlimited, then these spectra are well approximated with

$$\tilde{\Phi}(\omega;\mathbf{r}) \approx \Phi_0(\omega;\mathbf{r}) + \int_{\mathbf{r}'\epsilon\Omega}\frac{\delta c(\omega;\mathbf{r}')}{c_0(\omega)}K(\omega;\mathbf{r},\mathbf{r}')d^2\mathbf{r}' \tag{7}$$

where the complex sensitivity kernel is given by

$$K(\omega;\mathbf{r},\mathbf{r}') = 2k_0^2\tilde{\Phi}(\omega;\mathbf{r}')G(k_0;\mathbf{r},\mathbf{r}')w\left(\frac{\Delta'+\theta}{U}\right) \tag{8}$$

Here Δ' and θ are the running source-scatterer $\mathbf{r}'$ distance and scatterer-receiver $\mathbf{r}$ distance. It is assumed in equations (7) and (8) that the eigentaper is normalized by its peak value achieved at the group arrival time, i.e., $w(t_{\text{group}}) = 1$.

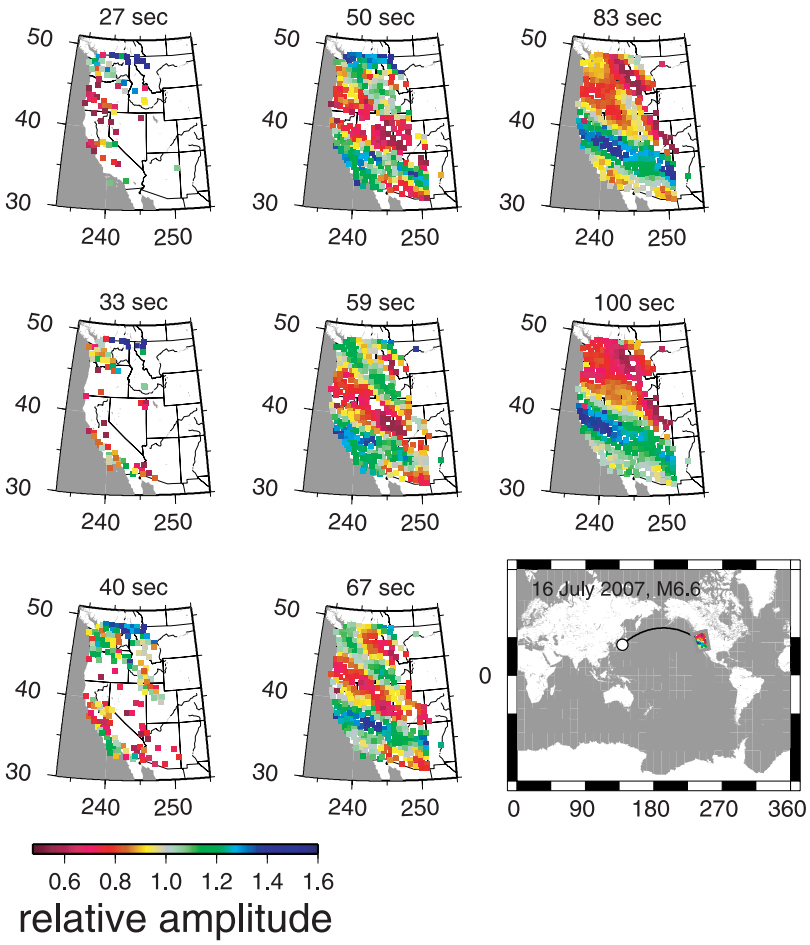

Figure 7. Relative amplitude of fundamental mode Rayleigh waves measured at Transportable Array sites at indicated periods for example event 4. Note that complex spectral amplitudes at periods <50 s were not included in further analysis because of the paucity of useful measurements at these periods.

4.2. Incident Wavefield

[16] Any superposition of spherical membrane waves arriving from arbitrary directions solves equation (6) and thus may represent Φ_0. Independent solutions available for this purpose are traveling wave Legendre functions $Q^{(1)}_{(\nu\ -\ 1/2)\mu}(\cos\theta)\ \exp(i\mu\phi)$ [*Dahlen and Tromp*, 1998, Appendix B], where $\nu = k_0$, θ and ϕ are the source-receiver distance and azimuth, respectively, and μ is arbitrary; it is convenient to have $\phi = 0$ coincide with the minor arc connecting the source to the center of the array. A practical way of synthesizing more complicated solutions is to take linear combinations of these functions over a continuum of μ as follows:

$$\Phi_0(\omega;\theta,\phi) = a_{-1}W_{-1}(\omega;\theta,\phi) + \sum_{l=0}^{l_{max}} a_l W_l(\omega;\theta,\phi)$$

$$W_{-1} = Q^{(1)}_{(\nu-1/2)0}(\cos\theta)$$

$$W_l = \int \left\{ h_l(\mu L)\exp\left[-\frac{(\mu L)^2}{2}\right]\right\}\left[Q^{(1)}_{(\nu-1/2)\mu}(\cos\theta)\exp(i\mu\phi)\right] \times (-\nu)^{-\mu}\exp\left(i\mu\frac{\pi}{2}\right)d\mu \qquad (9)$$

where h_l is a Hermite polynomial of degree l [*Abramowitz and Stegun*, 1972], L is a scale factor, and the a_l are complex constants. The a_{-1} term of equation (9) represents (the spherical equivalent of) a single plane wave arriving directly from the source back azimuth. The integrand factor $Q^{(1)}_{(\nu\ -\ 1/2)\mu}(\cos\theta)\ \exp(i\mu\phi)$ represents a plane wave arriving at an angle $\sin^{-1}\ (\mu/k_0)$ with respect to the source back azimuth. Example of the associated traveling wave Legendre functions $Q^{(1)}_{(\nu\ -\ 1/2)\mu}(\cos\theta)$ are presented in Figure S3. When θ is near $\pi/2$ (where the geometrical spreading factor has a local minimum), the solution of equation (9) coincides with the multiplane wave solution, i.e., W_l of equation (9) reduces to W_l of equation (10) of *Friederich and Wielandt* [1995]. Choosing $l_{\max} = 20$, all waves of practical interest may be generated by choosing $L = 9/k_0$ and μ integration limits from $-7/L$ to $+7/L$.

[17] Figure 12 shows the observed wavefield amplitudes for four events at period 50 s, together with the best fitting superposition of spherical membrane waves obtained from the iterative inversion (section 4.4). The calculated amplitude pattern captures to first order the lateral variations in the observed amplitude pattern. This demonstrates that most of the observed signal in the complex spectral amplitude measurements are part of the incident wavefield and a

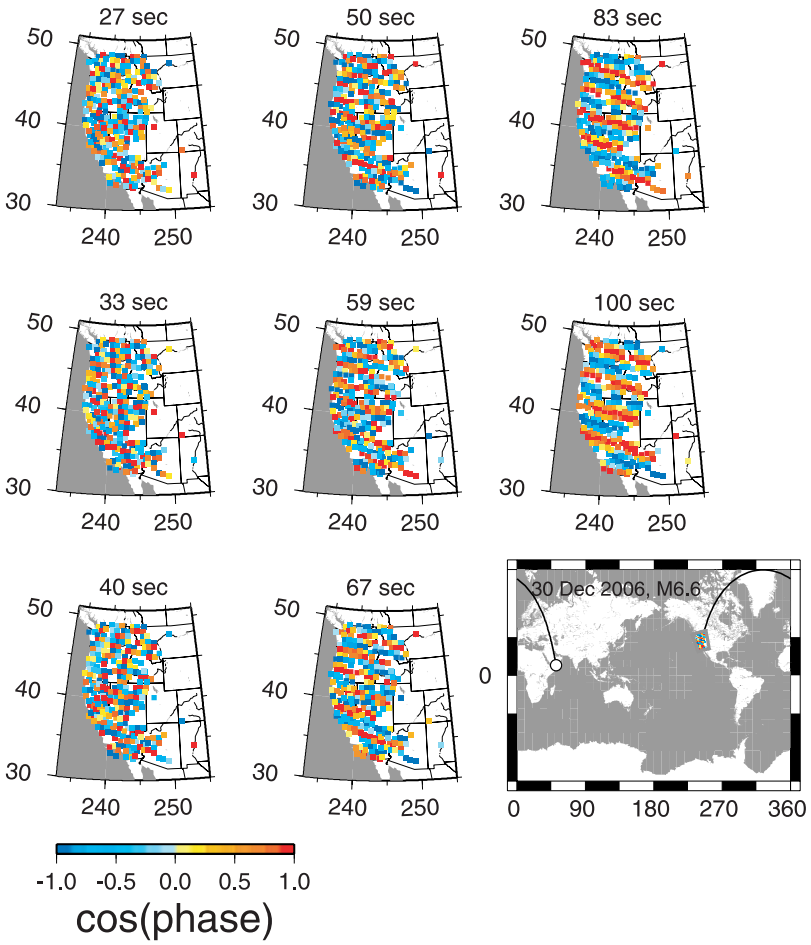

Figure 8. The cos ψ of fundamental mode Rayleigh waves measured at Transportable Array sites at indicated periods for example event 1.

relatively small remainder is generated by scattering interactions within the network area. A hint of the need for local surface wave scattering may be seen in the event 4 amplitude pattern. Along-propagation transitions from high to low amplitude in central Idaho (47°N, 113°E) and southern Arizona (32°N, 111°E) are indicative of relatively high phase velocity structure "upstream" from these regions, leading to defocussing "downstream."

[18] The interpretation method based on equation (7), with incident wavefields parameterized by equation (9), is designed to handle any incident wavefield, including those with a node in the radiation pattern across the TA. In practice, the automatic selection criteria tend to eliminate very low amplitude observations (e.g., Figure 7 at 50 s period). Since the basic observable is complex spectral amplitude, the presence of a node in the radiation pattern carries no special consequences for the phase velocity estimation.

[19] Figure S4 shows the basis wavefields W_l, $l = -1$, 0, ..., $l_{\max}$ for event 2 at period 50 s. In general, there are l nodes in the radiation pattern for W_l. The derived incident wavefield is a linear combination of these basis wavefields. Most of the power is concentrated in the plane wave ($l = -1$) and first two higher wavefields ($l = 0$, 1) (Figure S4).

4.3. Sensitivity Kernels for Amplitude and Phase

[20] From the complex sensitivity kernel given in equation (8) we may construct sensitivity kernels $K_{\delta\log(A)}$ and $K_{\delta\psi}$ on the aspherical model for surface wave amplitude and phase, respectively. Define a unit phase velocity perturbation at $\mathbf{r}_0$

$$\left(\frac{\Delta c}{c_0}\right)\delta(\mathbf{r}, \mathbf{r}_0) \tag{10}$$

to be superimposed on the aspherical model $\delta c(\omega; \mathbf{r})/c_0(\omega)$. Let $\delta\tilde{\Phi}(\omega; \mathbf{r}, \mathbf{r}_0)$ be the corresponding perturbation in $\tilde{\Phi}$. From equations (7) and (8) it follows that to first order in $(\Delta c/c_0)$, $\delta\tilde{\Phi}$ obeys the integral equation

$$\delta\tilde{\Phi}(\omega; \mathbf{r}, \mathbf{r}_0) = \left(\frac{\Delta c}{c_0}\right)K(\omega; \mathbf{r}, \mathbf{r}_0) + \int_{\mathbf{r}'\epsilon\Omega} \frac{\delta c(\omega; \mathbf{r}')}{c_0(\omega)}\delta K(\omega; \mathbf{r}, \mathbf{r}')d^2\mathbf{r}' \tag{11}$$

where

$$\delta K(\omega; \mathbf{r}, \mathbf{r}') = 2k_0^2\delta\tilde{\Phi}(\omega; \mathbf{r}', \mathbf{r}_0)G(k_0; \mathbf{r}, \mathbf{r}')w\left(\frac{\Delta' + \theta}{U}\right) \tag{12}$$

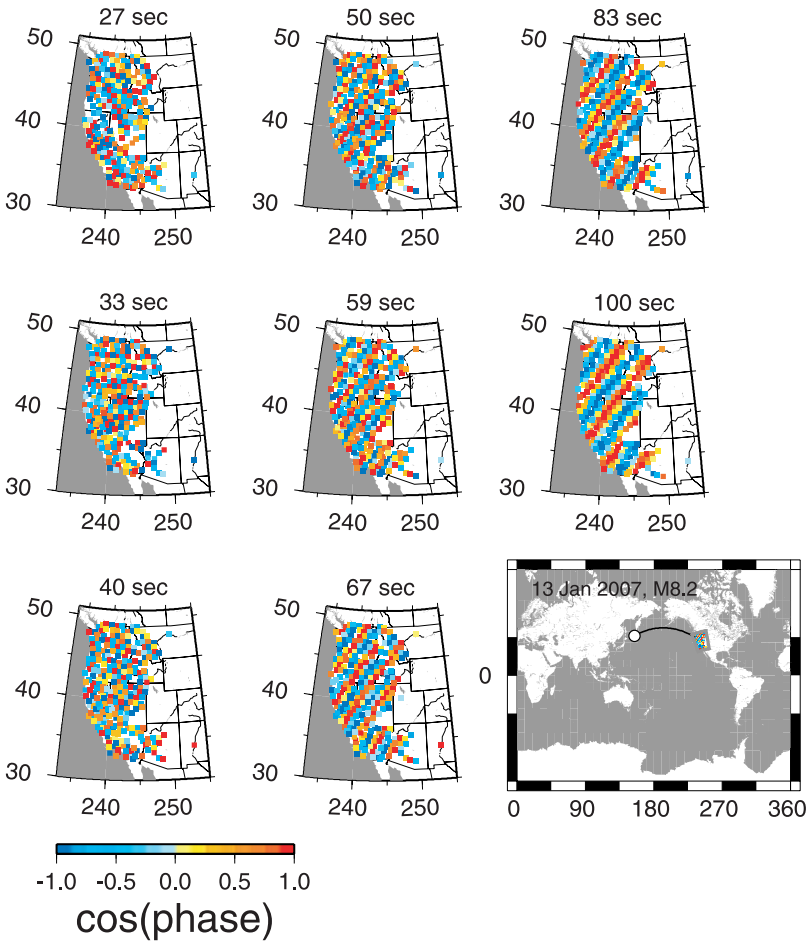

Figure 9. The cos ψ of fundamental mode Rayleigh waves measured at Transportable Array sites at indicated periods for example event 2.

[21] For the unit perturbation given in equation (10), the sensitivity kernels for amplitude and phase observed at $\mathbf{r}$ are

$$K_{\delta \log(A)}(\omega; \mathbf{r}, \mathbf{r}_0) = \lim_{\Delta c/c_0 \to 0} \frac{1}{\Delta c/c_0} \frac{\mathrm{Re}\left[\Phi^* \delta\tilde{\Phi}(\omega; \mathbf{r}, \mathbf{r}_0)\right]}{\Phi^* \Phi} \quad (13)$$

$$K_{\delta\psi}(\omega; \mathbf{r}, \mathbf{r}_0) = \lim_{\Delta c/c_0 \to 0} \frac{1}{\Delta c/c_0} \frac{\mathrm{Im}\left[\Phi^* \delta\tilde{\Phi}(\omega; \mathbf{r}, \mathbf{r}_0)\right]}{\Phi^* \Phi} \quad (14)$$

where asterisk denotes complex conjugation.

[22] It has been remarked [*Zhou et al.*, 2005] that 2-D sensitivity kernels for surface wave observables are inaccurate because they are typically bound by a forward scattering assumption. It is important to note that the 2-D sensitivity kernels defined here implicitly account for the effect of scattering angle on surface wave complex amplitudes. This follows from the fact that, assuming cross-branch coupling is neglected, scattering of a mode branch is governed by the Helmholz equation on a spherical membrane (i.e., equation (3)) with phase velocity given by equations (9) and (10) of *Pollitz* [1999]. The equivalence with an alternative solution exhibiting the dependence on scattering angle is shown in section 3.3 of *Pollitz* [1999]. Use of the exact solution of the spherical Helmholz equation (equation (4)) allows accurate estimation of phase velocity perturbation $\delta c(\omega; \mathbf{r}')$ and hence local phase velocity. Thus phase velocity maps derived from the spherical Helmholz equation in the present approach are not bound to the forward scattering assumption or the isotropic scattering assumption [*Friederich*, 1998]. The more serious issue is that of neglect of cross-branch coupling, which is common to many interpretation methods.

[23] Figure 13 shows examples of sensitivity kernels for the surface waves generated by event 3 (Figure 12) and recorded at station G15A. At all periods, the effect of a positive velocity perturbation along the central band is negative for $\delta\log(A)$ and positive for $\delta\psi$, corresponding to defocussing and a reduction in group arrival time (i.e., traveltime). In contrast with 3D sensitivity kernels of body wave traveltimes [e.g., *Dahlen et al.*, 2000; *Zhao et al.*, 2000], $K_{\delta\psi}$ for a 2-D perturbation is theoretically not zero along the direct raypath [*Zhou et al.*, 2004].

4.4. Solution of Integral Equation

[24] Iterative solution of the integral equation (4) is described by *Pollitz* [1999]. For a given seismic source and set of receivers, the steps are as follows:

[25] 1. $\tilde{\Phi}$ in equation (7) is fitted to observed $\tilde{\Phi}$ at a finite set of receivers $\{\mathbf{r}_i\}$ with $\delta c = 0$ and a single spherical membrane wave (the a_{-1} term of equation (9)) with origin

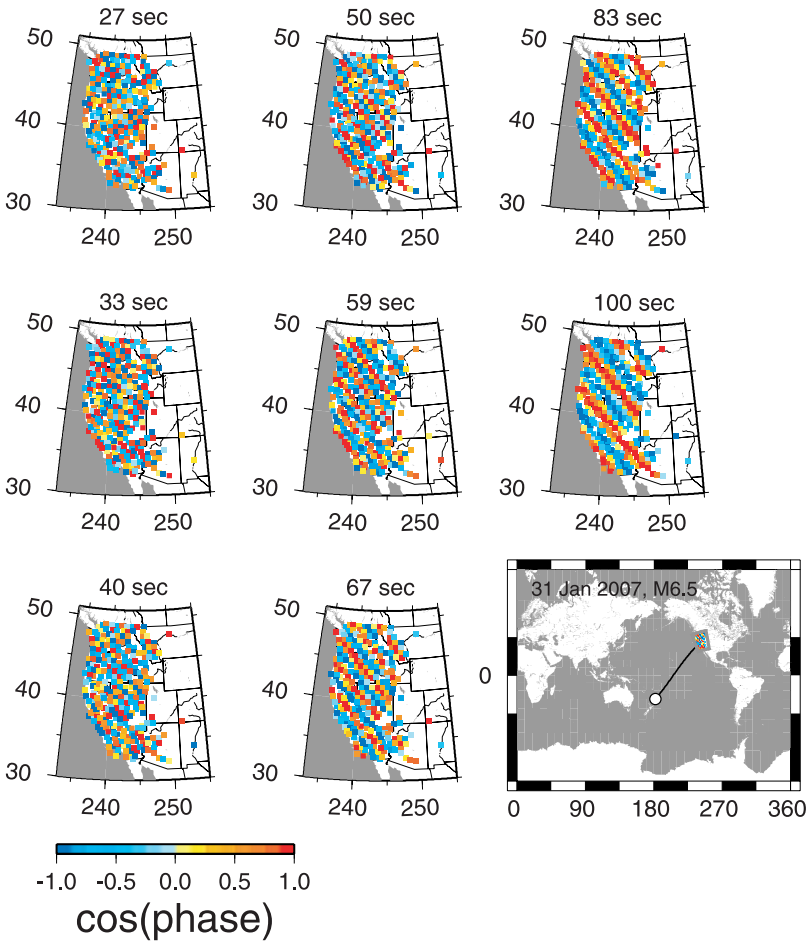

Figure 10. The cos ψ of fundamental mode Rayleigh waves measured at Transportable Array sites at indicated periods for example event 3.

at the source epicenter, with $c_0(\omega)$ adjusted to an optimal value in a grid search. $c_0(\omega)$ is hereafter fixed at this value. This step also yields an initial estimate of Φ_0.

[26] 2. Φ_0 is fixed at its previously determined value, and a suitably regularized δc is estimated by fitting $\tilde{\Phi}$ in equation (7) to observed $\tilde{\Phi}$.

[27] 3. δc is fixed at its previously determined value, and $\tilde{\Phi}$ in equation (7) is fitted to observed $\tilde{\Phi}$ by solving for Φ_0 with a suitably regularized superposition of spherical membrane waves, i.e., solving for the $\{a_l\}$ in equation (9). In addition to regularization (i.e., smoothing), the average amplitude of the observed wavefield and Φ_0 are constrained to be identical.

[28] 4. Steps 2 and 3 are repeated until convergence is achieved.

4.5. Results

[29] The above procedure is implemented at several periods T between 27 and 100 s. Smoothing weights for the regularization of phase velocity perturbation δc and the incident wavefields Φ_0 must be chosen [*Pollitz*, 1999]; smaller roughness in allowable Φ_0 trades off with greater roughness of estimated δc and vice versa. I chose these weights in such a way that at any period, about 90% of the initial variance in observed $\tilde{\Phi}$ was explained by a model of Φ_0 alone, and about 25–50% of the remaining variance explained by δc. This was found to yield incident wavefields not rougher than the observed wavefields and reasonably smooth phase velocity structures. The inverted phase velocity maps are not especially sensitive to the choice of wavefield damping parameter (α in equation (29) of *Pollitz* [1999]). Phase velocity maps at 50 s obtained using three different values of α, together with the corresponding incident wavefield amplitudes, for example, event 2, are shown in Figure S5. Greater α allows less signal to be absorbed by the incident wavefield and correspondingly more signal remaining to be explained with lateral phase velocity variations, resulting in greater amplitudes of phase velocity variations with increasing α. However, the pattern of phase velocity variation is robust.

[30] The distributions of sources used as a function of period (after editing the initial data set) are shown in Figure 14. The resulting phase velocity maps are shown in Figure 15. At relatively short wavelength ($\sim$100 km), the phase velocity maps generally agree with those obtained from ambient noise tomography at periods where they are comparable (ambient noise results up to 40 s are presented by *Yang and Ritzwoller* [2008] and at http://ciei.colorado.edu/$\sim$morganm/#dispersion_maps). In southern California, the phase velocity maps agree well with those of *Yang and Forsyth* [2006] based on two plane wave tomography, particularly at period of 27–50 s. At periods of 27–50 s

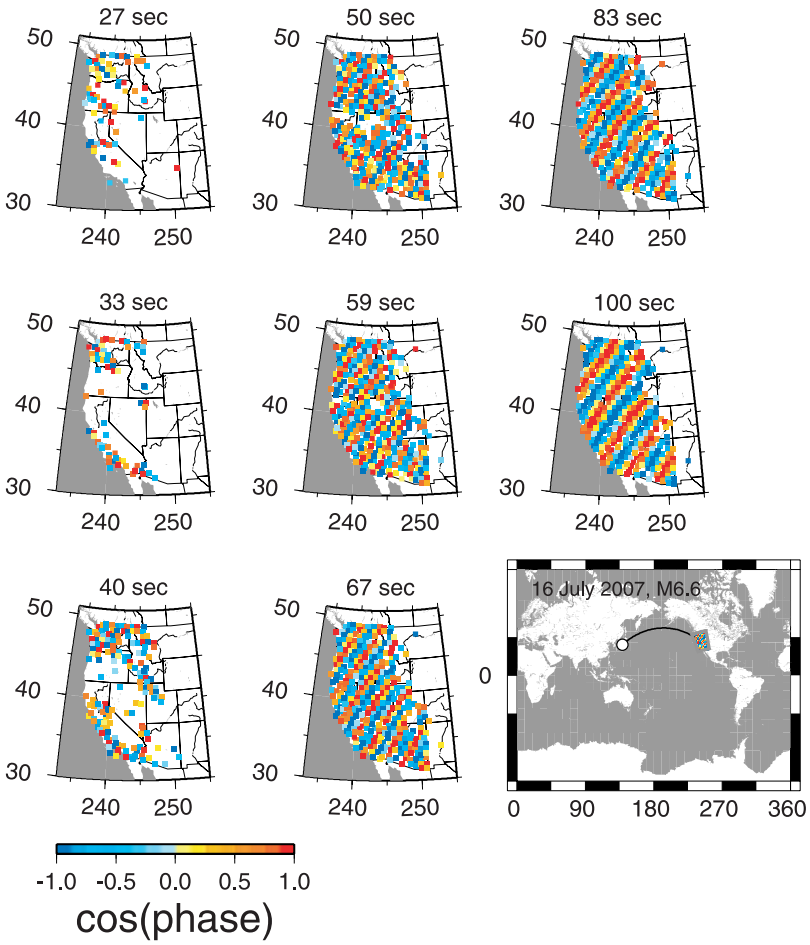

Figure 11. The cos ψ of fundamental mode Rayleigh waves measured at Transportable Array sites at indicated periods for example event 4.

they also agree well with phase velocity maps obtained by two-plane wave tomography applied separately to subsets of the TA [*Yang and Ritzwoller*, 2008]. At 67 and 100 s period, both the *Yang and Ritzwoller* [2008] (their Figure 4 at 66/100 s period) phase velocity maps and those in Figure 15 are highly correlated. However, the *Yang and Ritzwoller* [2008] phase velocity maps are much smoother than those obtained here. Since both studies are scattering-based and account for first-order complexity in the incident wavefields, differences are likely due to different parameterizations and regularizations between *Yang and Ritzwoller* [2008] and the present study. Common structure in the sets of phase velocity maps includes high velocity in the southern Great Valley, through north central California and central Oregon, and in central Washington, low velocity along eastern Nevada and eastern Washington, and a localized weak high-velocity region in north central Nevada. While these features are dominant in the phase velocity maps of *Yang and Ritzwoller* [2008], they are dwarfed in Figure 15 by phase velocity anomalies of +4 to +6% in western California and offshore around latitude 40°N. The same is true at 25/33 s period in the work by *Yang and Ritzwoller* [2008, Figure 3] and 27/33 s period in Figure 15: the phase velocity maps in the two studies are highly correlated, but those in Figure 15 exhibit local maxima of $\gtrsim$ +5% in the offshore region which are absent in the work by *Yang and Ritzwoller* [2008]. Thus the difference in results must also partially reflect the different domains of imaging used in the two studies.

[31] Figure 16 shows patterns of observed and modeled amplitude and phase at 50 s period. We define a first class of variance reductions with respect to complex spectral amplitudes $\tilde{\Phi}$, amplitudes $|\tilde{\Phi}|$, and phases $\Psi = \arg\Phi$. (In the case of a scalar such as amplitude or phase, variance measures the square of the quantity; in the case of a complex quantity, variance measures the sum of the squares of the real and complex parts.) A model of incident wavefields alone (i.e., Φ_0) achieves 85.3% variance reduction with respect to the

Figure 12. (right) Amplitude of observed 50 s fundamental mode Rayleigh waves (i.e., $|\tilde{\Phi}(\omega; \mathbf{r}_i)|$) across the TA for four example events. (left) Solution of equation (6) $\Phi_0(\omega; \mathbf{r})$, consisting of a superposition of spherical membrane waves designed to fit the observed complex spectral amplitudes simultaneously with laterally heterogeneous phase velocity structure. The inset shows teleseismic sources and paths to the TA from four example events: 1, 30 December 2006, M6.6; 2, 13 January 2007, M8.2; 3, 31 January 2007, M6.5; 4, 16 July 2007, M6.6.

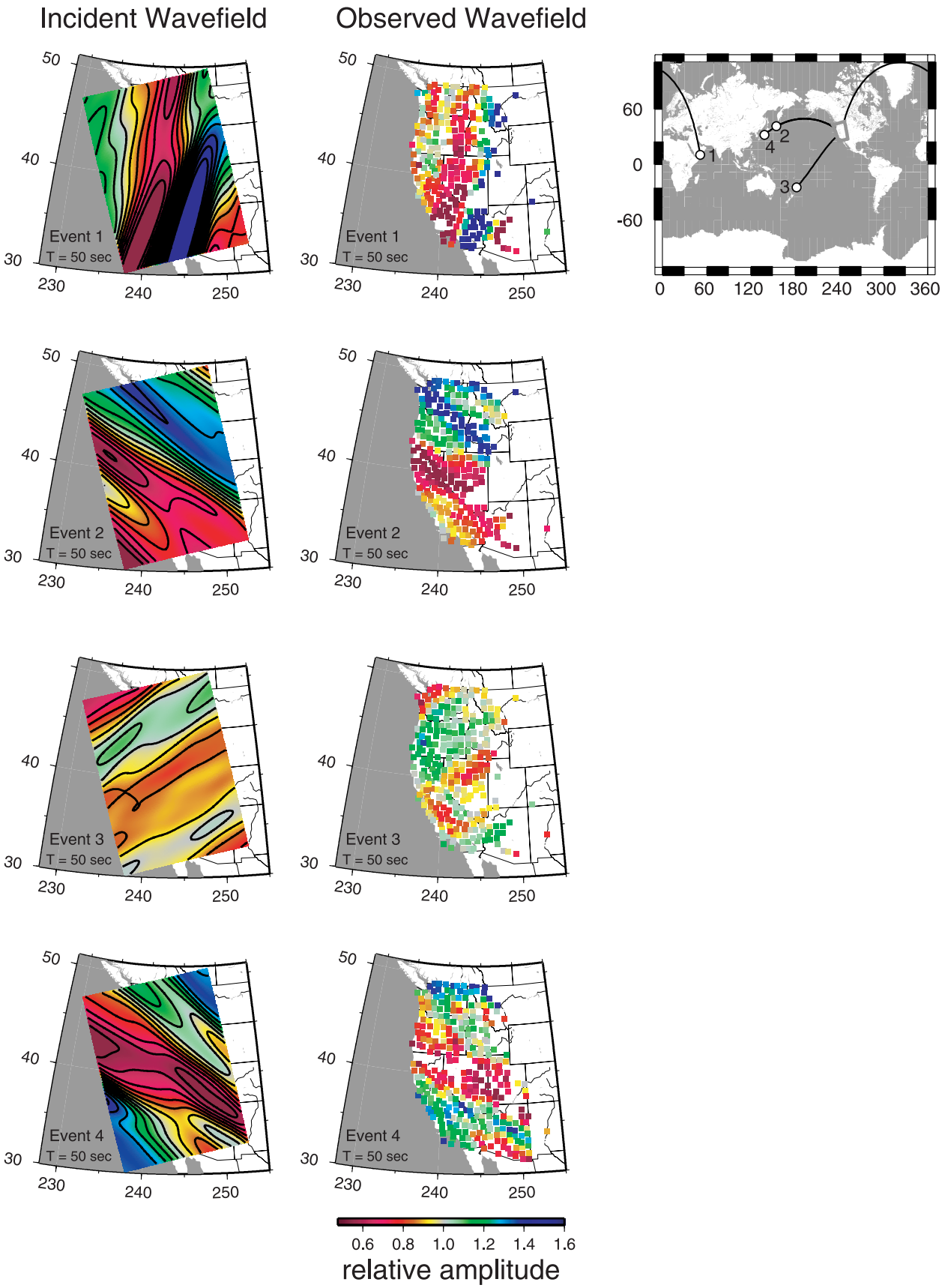
Incident Wavefield
Observed Wavefield
Event 1
T = 50 sec
Event 2
T = 50 sec
Event 3
T = 50 sec
Event 4
T = 50 sec
50
40
30
230
240
250
60
0
-60
0
60
120
180
240
300
360
1
2
3
4
0.6
0.8
1.0
1.2
1.4
1.6
relative amplitude

Figure 12

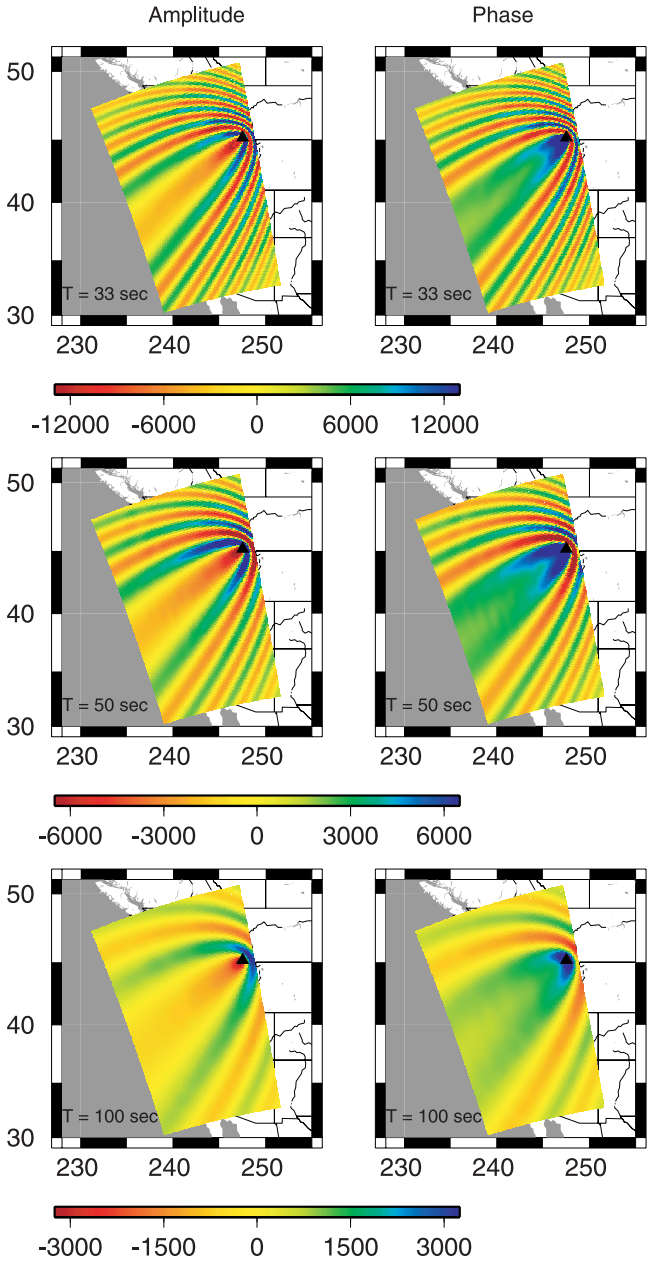

Figure 13. Sensitivity kernels for amplitude and phase $K_{\delta\log(A)}$ and $K_{\delta\psi}$ (equations (13) and (14)) for the 31 January 2007 event (Figure 12 inset) recorded by station G15A (indicated by triangle). Units are dimensionless.

complex amplitudes, 95.2% with respect to amplitudes, and 96.2% with respect to phases. We define a second class of variance reductions with respect to residual complex amplitudes $\tilde{\Phi} - \Phi_0$, residual amplitudes $|\tilde{\Phi}| - |\Phi_0|$, and residual phases $\Psi - \arg\Phi_0$, i.e., the residuals after subtracting a model of incident wavefields only. So defined, a model of seismic structure δc (which contributes to the spectral amplitude via the integral term of equation (7)) achieves an additional variance reduction of 45.4% with respect to the residual complex amplitudes, 8.2% with respect to the residual amplitudes, and 57.4% with respect to the residual phases. These patterns show that the incident wavefield explains a large fraction of the observed signal, and seismic structure explains about one half of the remaining signal, with most of the improvement due to alignment of surface wave phase.

[32] The scale of inverted velocity anomalies depends to a certain extent on the maximum degree l_{max} of the incident wavefield expansion used in equation (9). However, the cutoff degree is higher than required by any of the models, and the true controlling parameter is the damping factor applied to the structure (e.g., Figure S5). There is practically no difference in results between $l_{max} = 20$ (used in the models) and a smaller value of l_{max} (e.g., $l_{max} = 15$), indicating that most power in the expansion is at wavelengths considerably greater than the cutoff wavelength. This is verified by the falloff in the amplitude of the wavefield-weighting coefficients a_l as a function of l plotted in Figure S4.

4.6. Resolution

[33] Because the approach is scattering based and not based on ray theory, the lateral resolution of phase velocity in the present study is, in principle, unrestricted. Resolution tests (Figures S6–S11) indicate that a test structure with lateral variations on a 100–200 km scale may be recovered well at long period. Figures S5–S7 and S8–S10 show the inverted structures using two different sets of input structures. The inverted structures are obtained using the same regularizations as was applied to the TA data set. The coherence between input and inverted phase velocity structure diminishes sharply as period is reduced below ~40 s (Figure S12). Resolution at periods less than 27 s is compromised because, at shorter periods, the number of available sources is relatively few and there is a greater concentration of mode energy in the crust, leading to stronger scattering effects from structure both within and outside of the array [*Friederich et al.*, 1994]. This leads, in turn, to a greater ambiguity between the signal in the incident wavefields and that in the scattered wavefields. As the ability to discriminate their relative contributions diminishes, so diminishes the robustness of the scattered wavefields and correspondingly the inference of phase velocity structure.

4.7. Rayleigh Wave Dispersion

[34] The dispersion curve obtained from the measured average phase velocities as a function of period (Figure 17) is well fit by a PREM model appended by a 35 km thick continental crust and with reduced velocity in the asthenosphere (i.e., from the crust-mantle boundary to 220 km depth). A robust feature of this model, labeled WUS in Figure 17, is the 35 km thick crust. This is demanded by the 3.36 km/s and 3.43 km/s phase velocities at periods 18 s and 20 s (0.055 Hz and 0.050 Hz), respectively, at which periods the Rayleigh wave is sensitive primarily to crustal structure. Phase velocities are sensitive to Moho depth. A 1 km shallowing of the Moho increases phase velocities by 1% at these periods. Two models that have a crustal thickness of 25 km are included in Figure 17, representing the PREM and WUS models with reduced crustal thickness, and neither fits the observed dispersion. The employed average crustal thickness of 35 km agrees with regional studies based on receiver function analysis or refraction [e.g.,

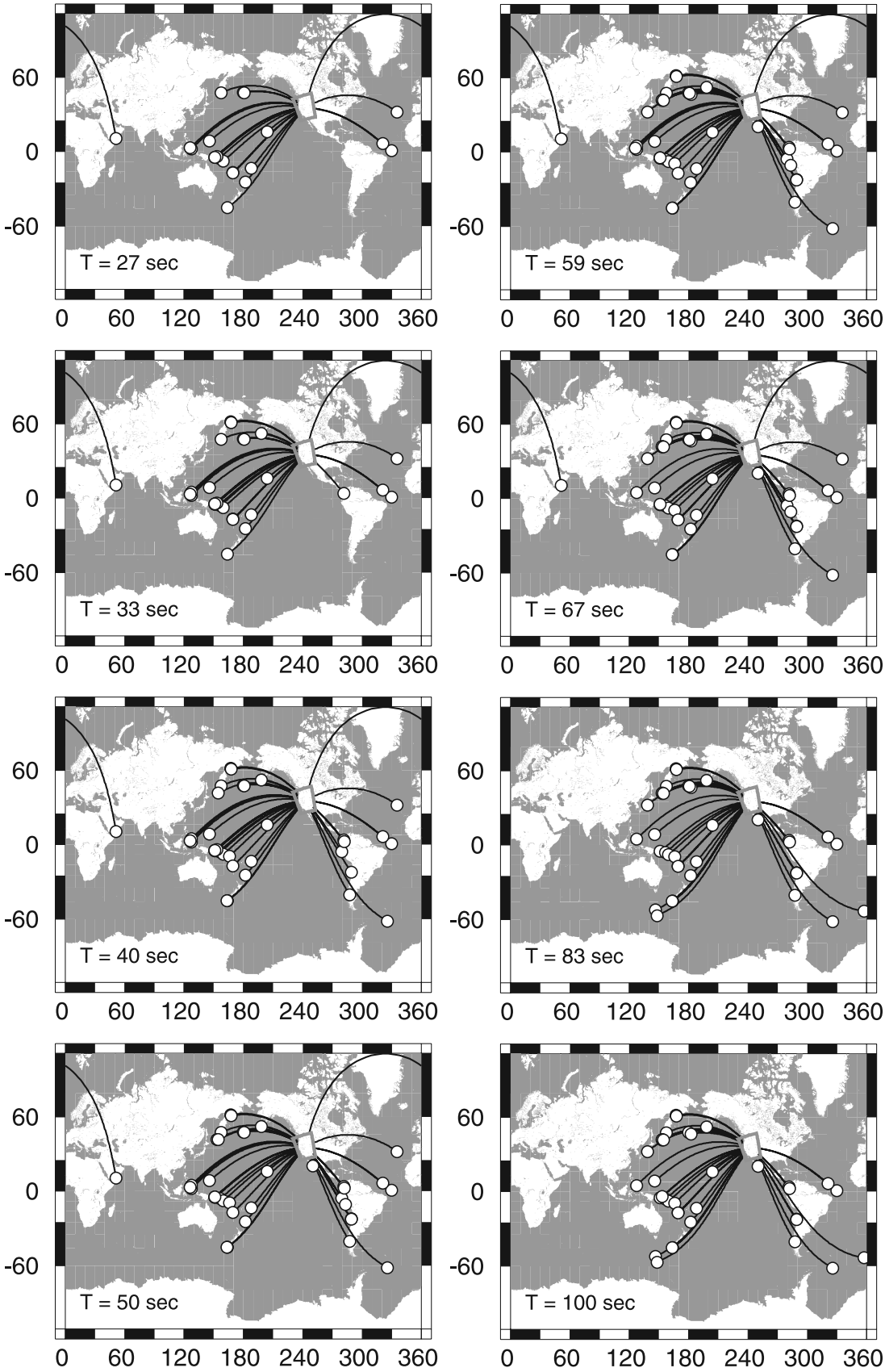

Figure 14. Distribution of teleseismic sources used in the inversion for phase velocity structure, as a function of period. The distributions vary from period to period because of selection criteria applied to the frequency-dependent measurements of complex spectral amplitudes [*Pollitz*, 1999]. Superimposed are the minor arc paths to the TA.

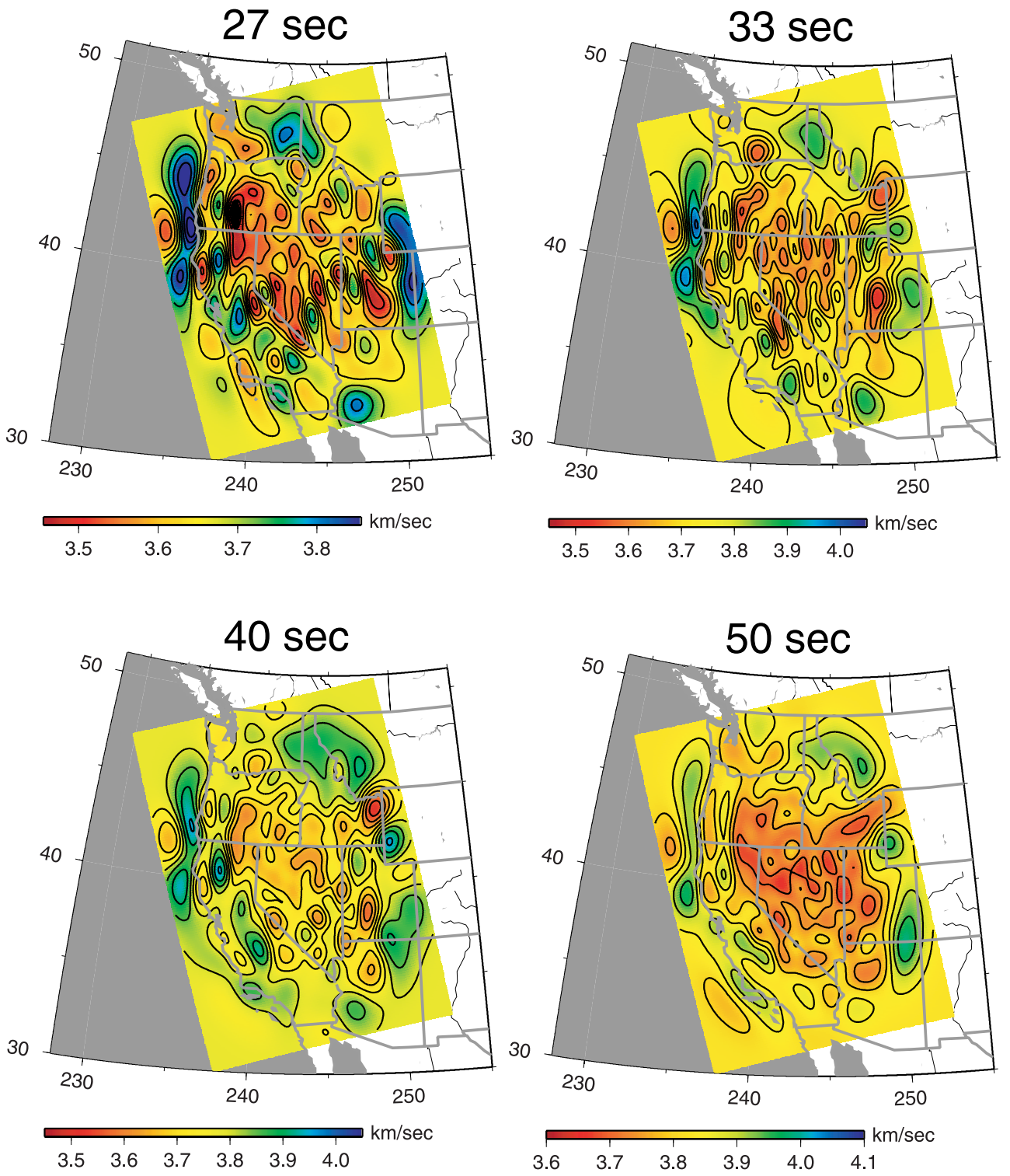

Figure 15. Rayleigh wave phase velocity maps at the indicated periods.

Prodehl, 1979; *Catchings and Mooney*, 1988; *Das and Nolet*, 1995; *Gilbert and Sheehan*, 2004; *Louie et al.*, 2004; *Heimgartner and Louie*, 2007].

4.8. Three-Dimensional Velocity Structure

[35] The WUS model serves as a reference spherically symmetric Earth model for a three-dimensional (3-D) structural inversion. The inversion for 3D structure assumes that phase velocity variations may be explained through perturbations with respect to a 1-D reference model. The use of a 1-D reference model is of course only approximate, and it would be more accurate to employ fully 3-D surface wave sensitivity kernels [e.g., *Zhou et al.*, 2004; *Tape et al.*, 2007].

[36] Phase velocity maps at periods of 27–100 s are inverted for the distribution of 3-D shear wave velocity v_s

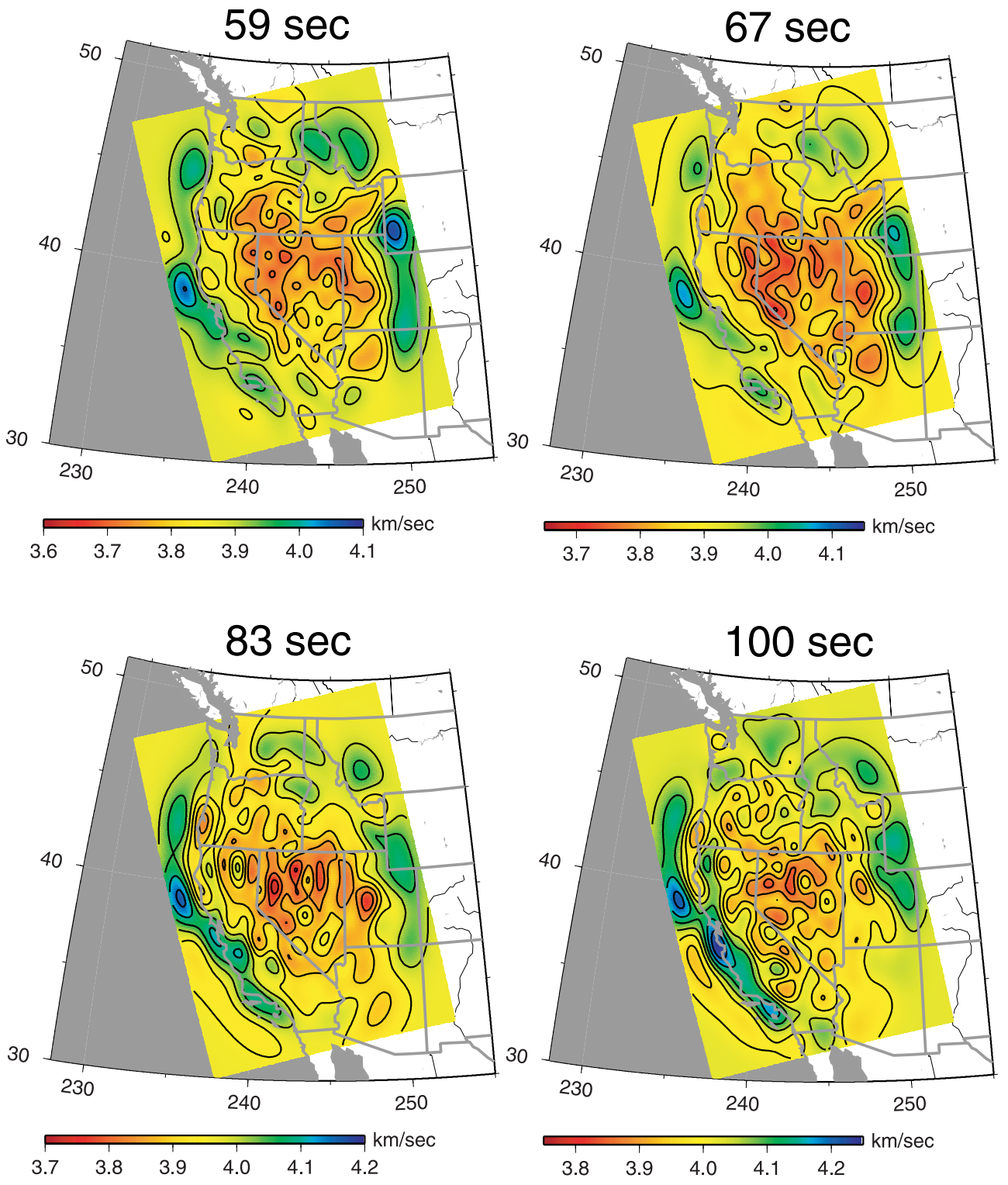

Figure 15. (continued)

following section 3.4 of *Pollitz* [1999], who assumes scaling relationships among perturbations in shear wave velocity v_s, compressional wave velocity v_p and density:

$$\frac{\delta\rho}{\rho} = 0.40\frac{\delta v_s}{v_s} \tag{15}$$

$$\frac{\delta v_p}{v_p} = 0.55\frac{\delta v_s}{v_s} \tag{16}$$

Inverted perturbations in v_s with respect to the reference model are shown in map views in Figures 18 and 19 and depth profiles in Figure 20. The v_s maps are highly correlated with seismic velocity maps based on body wave

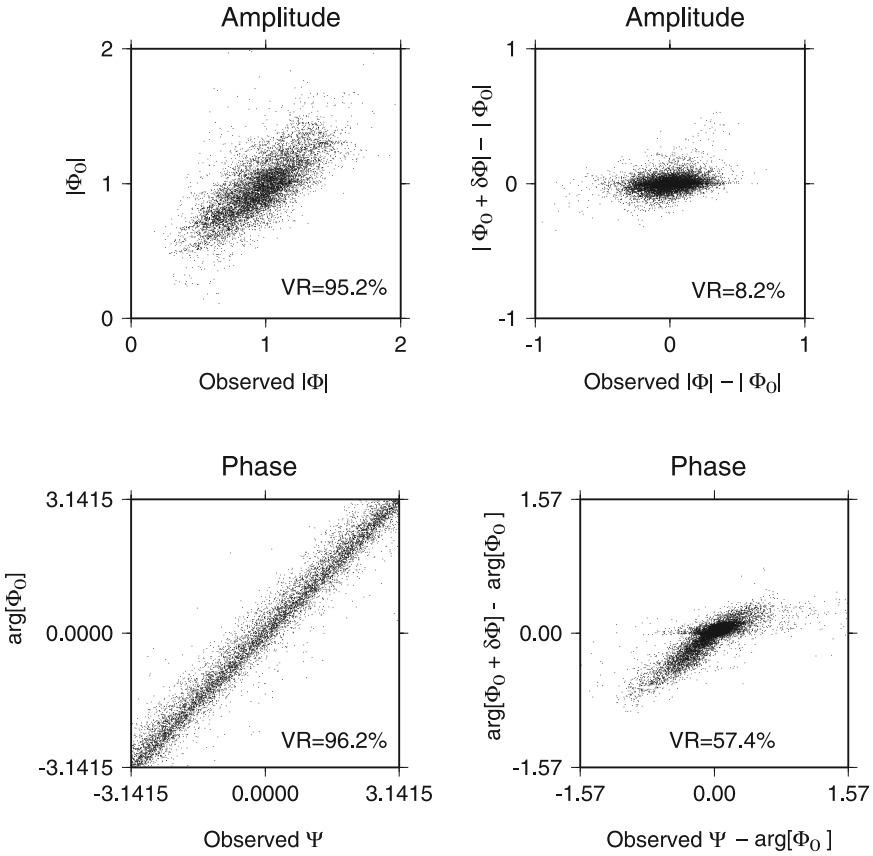

Figure 16. Constructs of relative amplitude $|\tilde{\Phi}|$ and phase Ψ at 50 s period using observed spectral amplitudes $\tilde{\Phi}$, the incident wavefields Φ_0, and the wavefields $\delta\tilde{\Phi}$ contributed by seismic structure (i.e., the integral term of equation (7)). A total of 8644 spectral amplitude measurements are represented in each plot. Amplitudes are scaled to average unity for each contributing seismic event. The variance reduction (VR) in each subplot pertains to the fit of the modeled quantity (y axis) with respect to the "observed" quantity (x axis). (left) Fit of the incident wavefield alone to the observed wavefield, and (right) improvement in fit by the addition of seismic structure.

tomography. For example, the v_s pattern at 110 km depth is comparable with the P wave velocity maps of *Bijwaard and Spakman* [2000] (plotted in Figure 8 of *Goes and van der Lee* [2002]), based on global P wave tomography, and *Dueker et al.* [2001], based on regional P wave tomography; both studies are based on three-dimensional ray tracing.

[37] The depth resolution is evaluated using synthetic phase velocity perturbations consisting of a 5% increase in shear velocity within a definite depth interval over the entire western United States, i.e., a spherically symmetric perturbation. The synthetic phase velocity distributions are then inverted in the same manner as the actual distributions. Figure 19 shows the inverted shear wave velocity structure for several 20 km thick input structures. It indicates that true structure over a narrow (e.g., 20 km) depth range is expected to be smeared over a broader depth interval with about one half the amplitude. It is clear that a smoother structure in depth may be more accurately recovered in terms of the inverted depth pattern and amplitude.

[38] Crustal thickness is assumed constant (35 km) in the 3D inversion, which implements only smooth variations in depth. Figure 19 indicates that lateral changes in crustal thickness may be mapped as smooth (in depth) velocity perturbations in the crust and uppermost mantle. This should be noted particularly in areas of high crustal thickness (Wyoming Craton, Colorado Plateau).

5. Discussion

[39] Salient features of the shear wave velocity distribution include: A deep-seated ($\gtrsim$ 100 km depth) velocity contrast across the San Andreas fault system (SAF; west side faster); a pronounced upper mantle velocity contrast across the Intermountain Seismic Belt (ISB) (east side in the Colorado Plateau and Rocky Mountains faster); low upper mantle velocities throughout the Basin and Range Province and Yellowstone–Snake River Plain; high velocities around associated with the oceanic lithosphere of the Juan de Fuca and Gorda plates; high upper mantle velocities beneath the southern Great Valley and Transverse Ranges; an upper mantle southern Nevada local velocity high which disrupts the low-velocity pattern of the surrounding Great Basin, and; reduced upper mantle velocities around the Coast Ranges just south of the Mendocino triple junction (40°N).

5.1. Juan de Fuca Slab

[40] Comparison of profiles AA', BB' and CC' suggests that the subducted Juan de Fuca slab dips more steeply

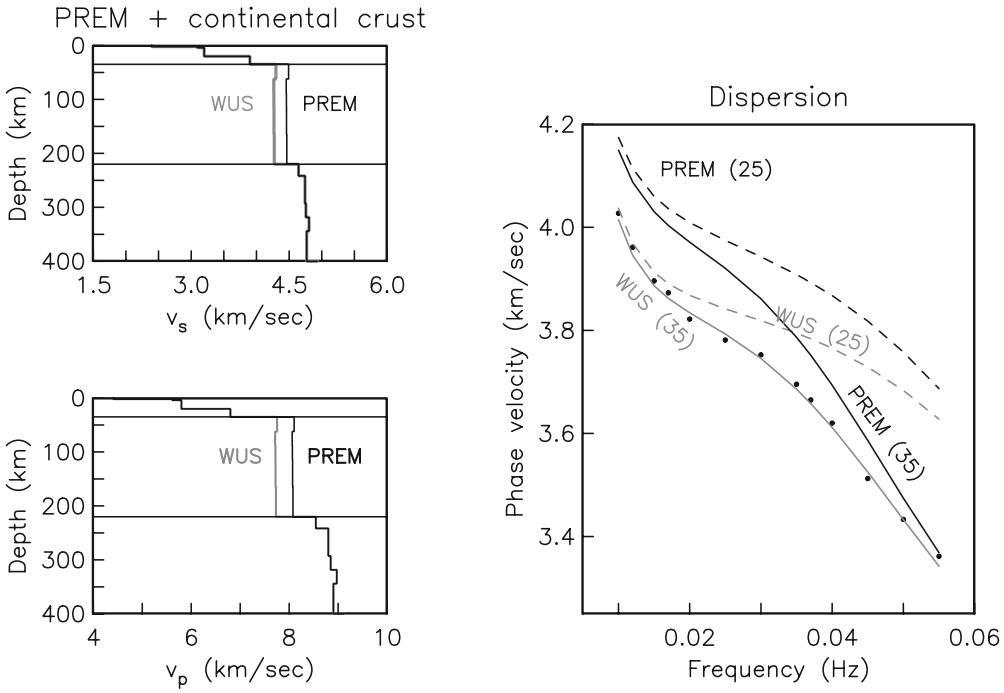

Figure 17. (left) PREM model [*Dziewonski and Anderson*, 1981] appended by a continental crust of thickness 35 km (solid black curve). The WUS model consists of 4.3% reduced velocity PREM in the asthenosphere (35–220 km depth) (solid gray curve). (right) Observed Rayleigh wave dispersion (filled circles) is compared with both the PREM model (black curves) and the WUS model (gray curves). Variations include PREM or WUS combined with a 25 km thick crust (dashed black and dashed gray curves, respectively), neither of which fits the observed dispersion.

below southern Washington and Oregon than beneath northern Washington. This pattern is consistent with the slab depth contours determined from microseismicity [*McCrory et al.*, 2004]. The Gorda slab is imaged near 40°N at depths $\gtrsim$ 30 km beneath the northern Sierra Nevada just south of the Mendocino triple junction (e.g., profile DD'). The contrast with respect to surrounding mantle persists to the depth of my model, and the Gorda slab is imaged to depths $\sim$ 300 km in body wave studies [*Dueker et al.*, 2001; *Humphreys and Dueker*, 1994]. The shallow portion of the slab is absent, and the adjacent Coast Ranges velocity low is thought to represent a mantle upwelling that fills a "slab window" left by the northward migrating Pacific-Juan de Fuca-North America triple junction [*Dickinson and Snyder*, 1979].

[41] Low-velocity upper mantle in the upper 100 km around 42°N, 127°W (Figure 18) is correlated with the Gorda Ridge (profiles BB' and CC' in Figure 20). Deeper than $\sim$ 100 km the low-velocity region yields to a region of high-velocity (profiles BB' and CC'), suggesting that the ridge behaves as a shallow structure not actively driven by deep asthenospheric flow. This is qualitatively similar to the structure beneath the Mid-Atlantic Ridge between latitudes 10°N and 60°N [*Silveira and Stutzmann*, 2002].

5.2. Farallon Slab Remnants

[42] Likely slab remnants from the former Farallon plate subduction may be traced intermittently as far south as the southern Great Valley (SGV; Figure 18), where the imaged high-velocity anomaly (profile EE') coincides with a high-velocity anomaly imaged to much greater depth in body wave studies [*Dueker et al.*, 2001; *Benz and Zandt*, 1993; *Humphreys and Dueker*, 1994; *Zandt*, 2003; *Boyd et al.*, 2004]. Another high-velocity anomaly beneath the western Transverse Ranges (WTR; 34.3°N, 120°W) is imaged to about 180 km depth using surface waves (profile FF') and $\sim$150–200 km depth using body waves [*Kohler et al.*, 2003; *Dueker et al.*, 2001; *Humphreys and Dueker*, 1994]. Both the SGV and WTR positive velocity anomalies as well as a Sierra Nevada and Walker Lane (SNWL) negative velocity anomaly (at about 36°N, 118°W and extending to the north-northwest in the 80 and 110 km depth slices) are also prominent features in the shear wave velocity images of *Yang and Forsyth* [2006, Figure 9]. However, a positive velocity anomaly beneath the eastern Transverse Ranges is imaged here only down to $\sim$ 90 km (profile FF') in contrast to $\sim$130 km in the work by *Yang and Forsyth* [2006] and $\sim$200 km in the work by *Kohler et al.* [2003]. The juxtaposition of the SGV anomaly with the SNWL anomaly to its east also agrees with the body wave tomography results of *Boyd et al.* [2004].

[43] The band of high-velocity material bounding the SAF on its west at depths $\sim$100–200 km is a striking feature of the longer-period phase velocity maps and 3D model (Figures 15 and 18 and profiles DD', EE', and FF' of Figure 20). Resolution is good along the entire stretch of this feature (Figures S6–S11); although it is to the west of essentially all TA stations, the large number of incident wave paths traversing the region (Figure 14) combined with the long-range sampling of the sensitivity kernels

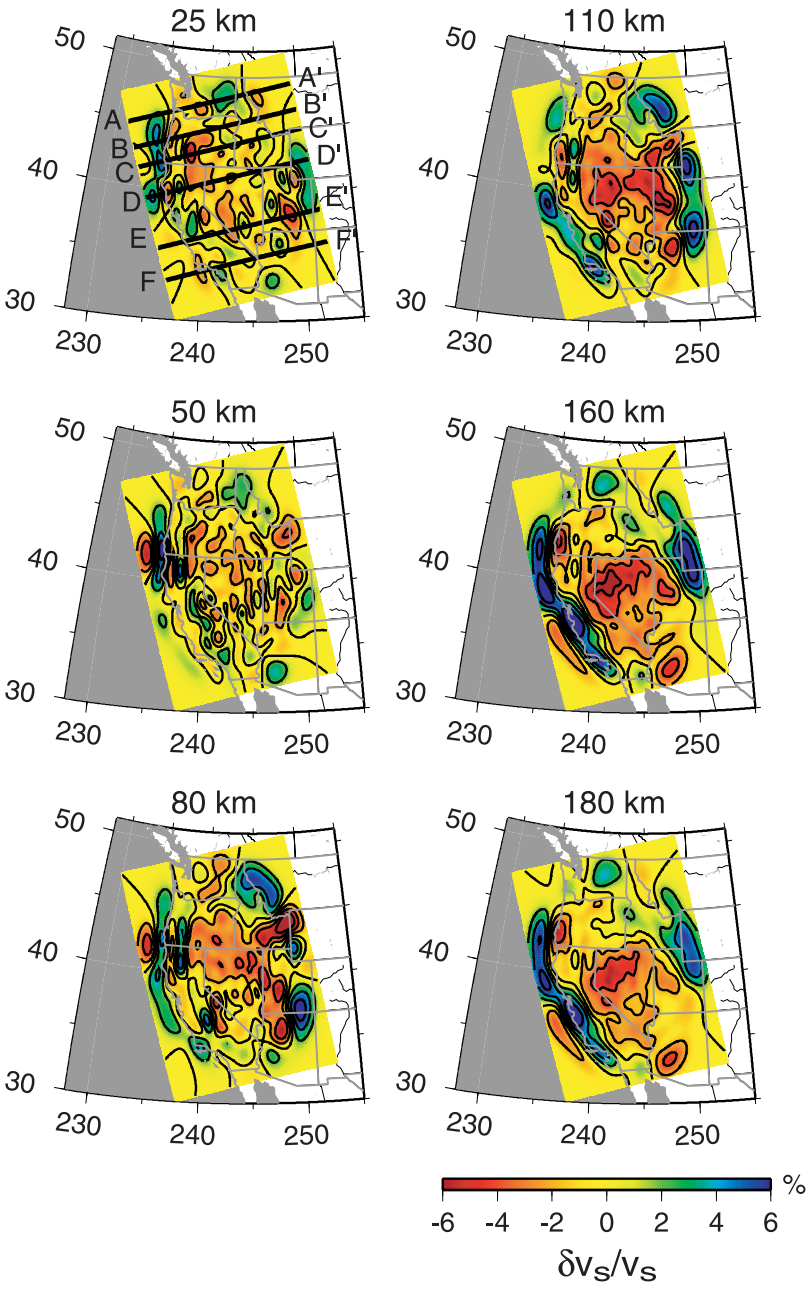

Figure 18. Perturbation in v_s with respect to the WUS reference model (Figure 17) in map views.

(Figure 13) leads to good resolution. Extending from the Mendocino triple junction (MTJ) to the California Borderland region in this depth range, it is not obviously connected with the Pacific plate lithosphere, which is expected to be not more than several 10s of km thick. I propose that it represents remnants of late stage Farallon plate lithosphere that was subducted between ~45–50 Ma B.P. and ~30–20 Ma B.P. The upper age range corresponds to the initiation of post-Laramide slab removal and slab reconfiguration, according to the model of *Humphreys* [1995]. The lower age range corresponds to the initiation of transcurrent motion on the SAF as the spreading ridges bordering the Farallon plate (and other microplates) impinged on the North American plate [*Atwater and Stock*, 1998]. *Humphreys* [1995] argues that newly subducted slab in the Pacific Northwest and California would have been decoupled from the previously subducted Farallon plate and therefore subducted with a steeper dip angle. He also argues that this facilitated subsequent slab rollback (which continues to the present time with the Juan de Fuca plate). I suggest that at any point south of the present MTJ, rollback of late stage Farallon subducted lithosphere, both before and after the transition to transcurrent motion on the SAF, led to the emplacement of this lithosphere west of the SAF. In this scenario, the remnant slab adjacent to the northern SAF would be older (≳ 30 Ma) than that adjacent to the southern SAF, where subduction of the Monterey and Arguello plates continued until about 20 Ma B.P. [*Atwater and Stock*, 1998]. In order to achieve its present extent, the remnant slabs would have necessarily been captured by the Pacific plate

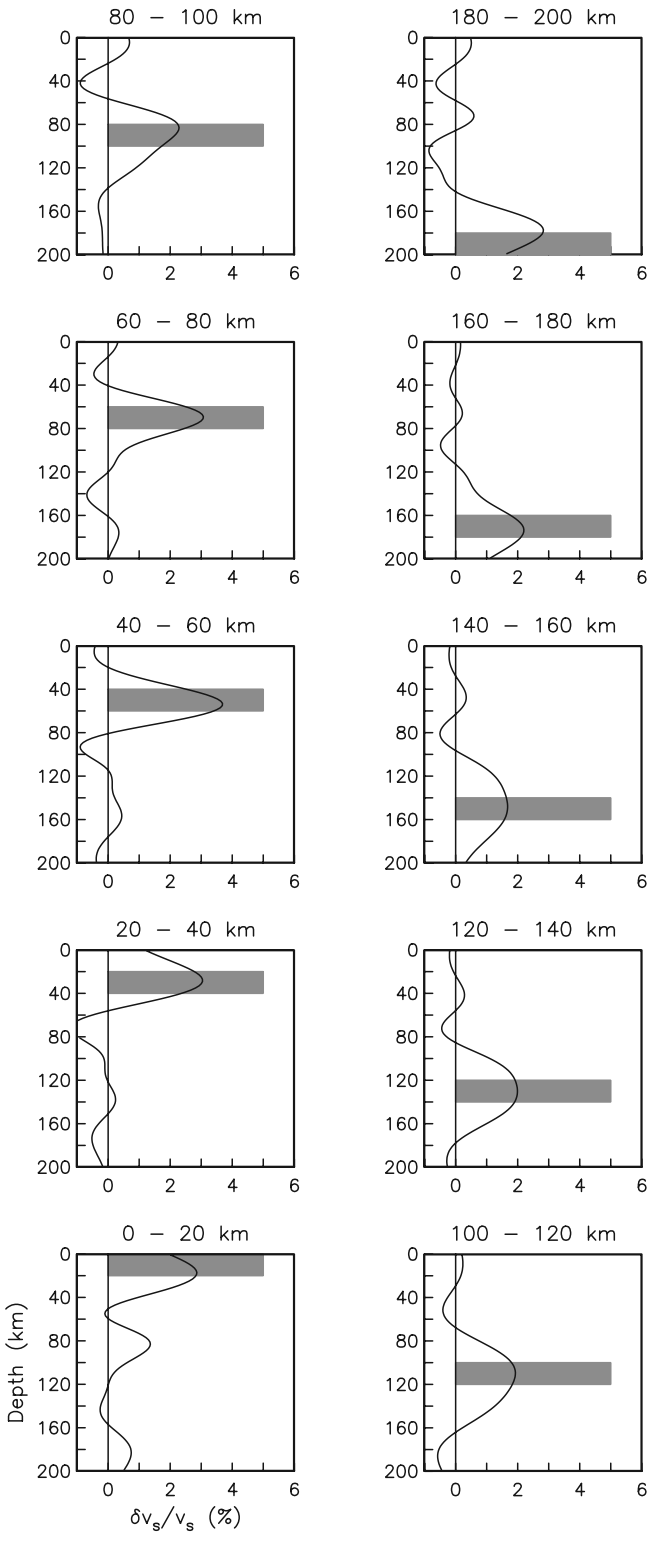

Figure 19. Inverted depth-dependent shear wave velocity using the indicated test structures in gray. These consist of a +5% shear wave velocity increase within a 20 km depth interval.

and transported northward, as proposed previously by *Benz and Zandt* [1993] for suspected remnant slab west of the SAF in central California. This idea was also proposed by *Bohannon and Parsons* [1995] on the basis of direct evidence from extinct spreading ridges off the California margin. They argued that the remnant Farallon slabs continued several hundred km east of the continental margin with a shallow (∼15°) dip. The present tomographic results would suggest that after capture up to 20 Ma ago, the slabs continued to rollback toward the ocean about an axis roughly coinciding with the SAF, then sank to their present positions just west of the SAF.

[44] A more recent analogue of the capture of Farallon microplates may be near the Gulf of California around latitude 24° to 28°N, where subduction of the Guadalupe and Magdalena plates ceased about 12 Ma B.P. [*Zhang et al.*, 2007]. Relatively high Rayleigh wave phase velocities at 50–100 s period west of the Gulf of California are interpreted by *Zhang et al.* [2007] as these stalled Farallon microplates.

5.3. Cratonic Lithosphere

[45] The eastern edge of the study area from the Colorado Plateau to the Wyoming Craton is generally high velocity and bounded by the eastern limit of the Sevier thrust belt, which coincides to a large extent with the ISB. The relatively low velocity layer overlying the Wyoming craton in profiles AA' and BB' indicates its large (∼ 53 km) crustal thickness [*Henstock et al.*, 1998; *Mueller and Frost*, 2006]. At ∼80–110 km depth under north central Idaho (Figure 18 and profiles AA' and BB' of Figure 20), the high-velocity pattern extends as far west as ∼ 116°W, coinciding with the Western Idaho Shear Zone (WISZ) [*Tikoff and McClelland*, 2005]. The WISZ also coincides with a sharp $^{87}Sr/^{86}Sr$ = .706 isopleth, with values > 0.7055 and < 0.7043 on the east and west sides, respectively [*Armstrong et al.*, 1977]. It represents a sharp transition at the edge of the pre-Mesozoic continental margin. Low-velocity crust overlying the high-velocity basement in south central Idaho and western Montana appears to correlate with the Idaho Batholith [*Hyndman*, 1983] (profiles BB' and CC' of Figure 20), although further resolution of this feature must await more detailed seismic experiments.

5.4. Great Basin

[46] The velocity pattern throughout the Great Basin confirms the view that the Great Basin is generally underlain by hot and buoyant mantle [e.g., *van der Lee and Nolet* 1997], but it also reveals additional detail. The low shear wave velocities in northern Nevada, southeast Oregon, and southwest Idaho (e.g., at 110 km depth in Figure 18) correlate with large thermal elevation [*Lowry et al.*, 2000], suggesting that they are associated with thermal perturbations. The systematic sharp velocity contrast across the ISB is matched by a sharp contrast in effective elastic plate thickness [*Lowry et al.*, 2000]. The "southern Nevada anomaly" appears consistently in Figure 18 as a localized (∼ 200–400 km radius), relatively high velocity area. In profile EE', it is mapped as a relatively high velocity area at depths ≲ 110 km. Its position near 37.5°N, 116°W is just east of the junction of four prominent seismic zones (Figure 2): the ECSZ, WLSB, CNSZ, and SNTZ. Since it is also associated with low heat flow [*Humphreys et al.*, 2003], I suggest that this velocity anomaly represents an entrapped piece of relatively thick lithosphere within the Great Basin that helps to concentrate seismic activity along

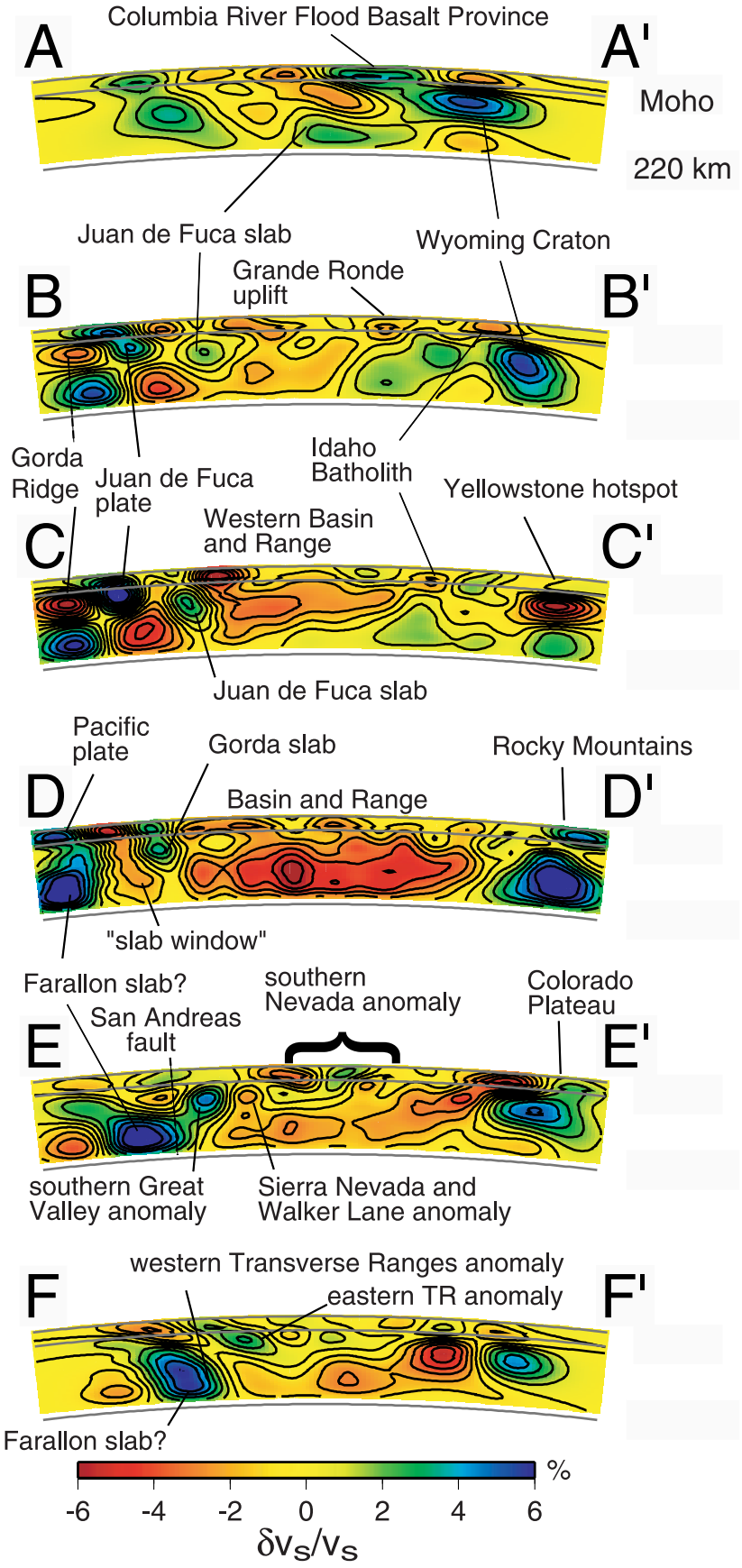

Figure 20. Perturbation in v_s with respect to the WUS reference model (Figure 17) in depth profiles. Profiles locations are shown in Figure 18.

its western and southern borders. It includes the southern Nevada "amagmatic gap" of the central Basin and Range, which bounds southward and northward advancing fronts of Miocene volcanism [*Faulds et al.*, 2001; *Eaton*, 1982]. It may have played the role of a stress guide between the subducting Farallon plate (to its southwest) and the areas of crustal shortening in Colorado and Wyoming during the Laramide Orogeny [*Humphreys et al.*, 2003; *Saleeby*, 2003].

[47] Relatively thin lithosphere in most of the Great Basin may be of thermal origin (thermal thinning of the lithosphere) or compositional origin arising from greater hydration of the mantle, consistent with the fact that high water concentrations may decrease seismic velocities [*Karato*, 2004]. A combination of both seems likely given that most of the present Great Basin was subjected to Farallon slab removal from ~50 to 20 Ma, emplacing asthenosphere adjacent to the crust [*Humphreys*, 1995]. Greater hydration of the western U.S. mantle during Farallon plate subduction is expected to have decreased the viscosity, increased the mobility and led to a greater degree of advected heat transport [*Hyndman et al.*, 2005].

5.5. Yellowstone Anomaly

[48] The Yellowstone low-velocity anomaly is imaged to no deeper than ~ 150 km (profile CC'). This agrees with the inference from short-period P wave tomography that the Yellowstone anomaly does not extend below 150–200 km depth [*Christiansen et al.*, 2002] and the absence of a detectable velocity anomaly using finite frequency tomography [*Montelli et al.*, 2004]. However, the surface wave tomography does not rule out the possibility of a weaker low-velocity anomaly proposed to dip steeply toward the northwest from the Yellowstone caldera, extending to $\gtrsim$ 400 km depth [*Waite et al.*, 2006].

5.6. Mantle Delamination

[49] Areas of likely recent mantle delamination and associated uplift are the Wallowa mountains of northwest Oregon [*Hales et al.*, 2005] and the southern Sierra Nevada Range [*Saleeby and Foster*, 2004]. Each of these areas is underlain by low-velocity mantle, from ~35 to 50 km beneath the Grande Ronde uplift, Wallowa mountains (profile BB') and $\gtrsim$ 50 km beneath the southern Sierra Nevada (profile EE'), consistent with upwelling asthenosphere beneath the uplifts. The shallow low-velocity mantle yields to relatively high-velocity mantle at $\gtrsim$ 100 km beneath the Grande Ronde uplift, in good agreement with Figure 3b of *Hales et al.* [2005] and consistent with their interpretation of convective mantle downwelling.

[50] Prior to delamination, the Wallowa region may have shared the high-velocity crust and uppermost mantle of the Columbia Plateau in eastern Washington (profile AA'). This velocity structure is similar to that of many large igneous provinces [*Coffin and Eldholm*, 1994].

6. Conclusions

[51] I measure the spectral amplitudes of fundamental mode Rayleigh waves from 18 months of long-period seismic recordings by the Transportable Array. The approximately 400-station array yields unprecedented images of long-period seismic surface wavefields. The surface wavefields generated by shallow focus teleseismic events have generally complicated amplitude patterns but very simple phase patterns, suggesting that focussing and multipathing are capable of highly distorting surface wave amplitudes even when the wavefronts themselves are smooth.

[52] Finite frequency multiplane surface wave tomography is applied to the TA data set. By jointly estimating incident surface wavefields for every teleseismic event and phase velocity structure for every teleseismic event, the signal contributed by the latter is more effectively isolated. Phase velocity distributions are estimated from 27 to 100 s period and reveal structural details of western U.S. upper mantle structure across a $\sim 2000 \times 1400$ km^2 area down to ~200 km depth. Prominent structures identified in the surface wave tomography generally agree with the results of body wave tomography, though the estimated depth extent of surface wave anomalies is often shallower. This reflects both the limited period range and limited resolving power of surface waves with depth. The seismic structure of the western United States is obtained with only a small fraction of the information provided by the Transportable Array. Even deeper and sharper images are expected to result from future studies integrating surface wave and body wave observations.

[53] **Acknowledgments.** Source locations and magnitudes are from the NEIC catalog. Data from the Transportable Array were provided by the Incorporated Research Institutions for Seismology (IRIS) Data Management Center. I thank Tom Brocher and Bill Ellsworth for their comments on a preliminary draft and Richard Allen, John Evans, Gene Humphreys, David James, Thorne Lay, Pat McCrory, Barbara Romanowicz, Arthur Snoke, and Wayne Thatcher for insightful discussions. This paper benefitted from the constructive criticisms of Donald Forsyth and two anonymous reviewers.

References

Abramowitz, M., and I. Stegun (1972), *Handbook of Mathematical Functions*, vol.1, U. S. Dep. Commer., Natl. Bureau of Stand., Washington, D. C.

Armstrong, R. L., W. H. Taubeneck, and P. O. Hales (1977), Rb-Sr and K-Ar geochronology of Mesozoic granitic rocks and their Sr isotopic composition, Oregon, Washington, and Idaho, *Geol. Soc. Am. Bull.*, *88*, 397–411.

Atwater, T., and J. Stock (1998), Pacific-North America plate tectonics of the Neogene southwestern United States—An update, *Int. Geol. Rev.*, *40*, 375–402.

Baig, A. M., and F. A. Dahlen (2004), Statistics of traveltimes and amplitudes in random media, *Geophys. J. Int.*, *158*, 187–210.

Benz, H. M., and G. Zandt (1993), Lithospheric structure of the San Andreas fault system in northern and central California, in *Seismic Tomography*, edited by H. M. Iyer and K. Hirahara, pp. 440–465, Chapman and Hall, New York.

Bijwaard, H., and W. Spakman (2000), Non-linear global P-wave tomography by iterated linearized inversion, *Geophys. J. Int.*, *141*, 71–82.

Bohannon, R. G., and T. Parsons (1995), Tectonic implications of post-30 ma Pacific and North American relative plate motions, *Geol. Soc. Am. Bull.*, *107*, 937–959.

Boyd, O. S., C. H. Jones, and A. F. Sheehan (2004), Foundering lithosphere imaged beneath the southern Sierra Nevada, *Science*, *305*, 660–662.

Catchings, R. D., and W. D. Mooney (1988), Crustal structure of the Columbia Plateau: Evidence for continental rifting, *J. Geophys. Res.*, *93*, 459–474.

Christiansen, R. L., G. R. Foulger, and J. R. Evans (2002), Upper-mantle origin of the Yellowstone hotspot, *Geol. Soc. Am. Bull.*, *114*, 1245–1256.

Coffin, M. F., and O. Eldholm (1994), Large igneous provinces: Crustal structure, dimension, and external consequences, *Rev. Geophys.*, *32*, 1–36.

Dahlen, F. A. (1980), A uniformly valid asymptotic representation of normal multiplet spectra on a laterally heterogeneous Earth, *Geophys. J. R. Astron. Soc.*, *62*, 225–247.

Dahlen, F. A., and J. Tromp (1998), *Theoretical Global Seismology*, Princeton Univ. Press, Princeton, N. J.

Dahlen, F. A., S. H. Hung, and G. Nolet (2000), Fréchet kernels for finite-frequency traveltimes-I. Theory, *Geophys. J. Int.*, *141*, 157–174.
Das, T., and G. Nolet (1995), Crustal thickness estimation using Rayleigh waves, *Geophys. Res. Lett.*, *22*, 539–542.
Dickinson, W. R., and W. S. Snyder (1979), Geometry of subducted slabs related to the San Andreas transform, *J. Geol.*, *87*, 609–627.
Dokka, R. K., and C. J. Travis (1990), Role of the Eastern California shear zone in accommodating Pacific-North America plate motion, *Geophys. Res. Lett.*, *17*, 1323–1326.
Dueker, K., H. Yuan, and B. Zurek (2001), Thick-structured Proterozoic lithosphere of the Rocky Mountain region, *GSA Today*, *11*, 4–9.
Dziewonski, A., and D. Anderson (1981), Preliminary reference Earth model, *Phys. Earth Planet. Inter.*, *25*, 297–356.
Eaton, G. P. (1982), The Basin and Range Province: Origin and tectonic significance, *Annu. Rev. Earth Planet. Sci.*, *10*, 409–440.
Faulds, J., D. Feuerbach, C. Miller, and E. Smith (2001), Cenozoic evolution of the northern Colorado River extensional corridor, southern Nevada and northwest Arizona, in *The Geologic Transition, High Plateaus to Great Basin: A Symposium and Field Guide, Publ. GB 78*, edited by M. C. Erskine et al., pp. 239–272, Pac. Sect., Am. Assoc. of Pet. Geol., Bakersfield, Calif.
Friederich, W. (1998), Wave-theoretical inversion of teleseismic surface waves in a regional network: Phase velocity maps and a three-dimensional upper-mantle shear-wave velocity model for southern Germany, *Geophys. J. Int.*, *132*, 203–225.
Friederich, W., and E. Wielandt (1995), Interpretation of seismic surface waves in regional networks: Joint estimation of wavefield geometry and local phase velocity method and numerical tests, *Geophys. J. Int.*, *120*, 731–744.
Friederich, W., E. Wielandt, and S. Stange (1994), Non-plane geometries of seismic surface wavefields and their implications for regional-scale surface-wave tomography, *Geophys. J. Int.*, *119*, 931–948.
Gilbert, H., and A. Sheehan (2004), Images of crustal variations in the intermountain west, *J. Geophys. Res.*, *109*, B03306, doi:10.1029/2003JB002730.
Goes, S., and S. van der Lee (2002), Thermal structure of the North American uppermost mantle inferred from seismic tomography, *J. Geophys. Res.*, *107*(B3), 2050, doi:10.1029/2000JB000049.
Hales, T. C., D. L. Abt, E. D. Humphreys, and J. J. Roering (2005), A lithospheric instability origin for Columbia River flood basalts and Wallowa Mountains uplift in northeast Oregon, *Nature*, *438*, 842–845.
Heimgartner, M., and J. N. Louie (2007), Using seismic refraction to assess geothermal potential: An updated view of crustal thickness in the Great Basin, *Geotherm. Resour. Counc. Trans.*, *31*, 121–124.
Henstock, T. J., et al. (1998), Probing the Archaen and Proterozoic lithosphere of western North America, *GSA Today*, *8*, 1–5.
Humphreys, E. (1995), Post-Laramide removal of the Farallon slab, western United States, *Geology*, *23*, 987–990.
Humphreys, E., and K. Dueker (1994), Western US upper mantle structure, *J. Geophys. Res.*, *99*, 9615–9634.
Humphreys, E., E. Hessler, K. Dueker, G. L. Farmer, E. Erslev, and T. Atwater (2003), How Laramide-age hydration of North American lithosphere by the Farallon slab controlled subsequent activity in the western United States, *Int. Geol. Rev.*, *45*, 575–595.
Hung, S. H., F. A. Dahlen, and G. Nolet (2001), Wavefront healing: A banana-doughnut perspective, *Geophys. J. Int.*, *146*, 289–312.
Hyndman, D. W. (1983), The Idaho batholith and associated plutons, Idaho and western Montana, in *Circum-Pacific Plutonic Terranes*, edited by J. A. Roddick, *Mem. Geol. Soc. Am.*, *159*, 213–240.
Hyndman, R. D., C. A. Currie, and S. P. Mazzotti (2005), Subduction zone backarcs, mobile belts, and orogenic heat, *GSA Today*, *15*, doi:10:1130/1052-5173.
Karato, S. (2004), Mapping water content in the upper mantle, in *Inside the Subduction Factory*, *Geophys. Monogr. Ser.*, vol. 138, edited by J. Eiler, pp. 135–152, AGU, Washington, D. C.
Kohler, M. D., H. Magistrale, and R. W. Clayton (2003), Mantle heterogeneities and the SCEC reference three-dimensional seismic velocity model version 3, *Bull. Seismol. Soc. Am.*, *93*, 757–774.
Louie, J. N., W. Thelen, S. B. Smith, J. B. Scott, M. Clark, and S. Pullammanappallil (2004), The northern Walker Lane refraction experiment: Pn arrivals and the northern Sierra Nevada root, *Tectonophysics*, *388*, 253–269.
Lowry, A. R., N. M. Ribe, and R. B. Smith (2000), Dynamic elevation of the Cordillera, western United States, *J. Geophys. Res.*, *105*, 23,371–23,390.
McCrory, P. A., J. L. Blair, D. H. Oppenheimer, and S. R. Walter (2004), Depth to the Juan de Fuca slab beneath the Cascadia subduction margin—A 3-D model for sorting earthquakes, *USGS Data Ser., DS-91*, version 1.2.
Montelli, R., G. Nolet, F. A. Dahlen, G. Masters, E. R. Engdahl, and S.-H. Hung (2004), Finite-frequency tomography reveals a variety of plumes in the mantle, *Nature*, *303*, 338–343.
Mueller, P. A., and C. D. Frost (2006), The Wyoming Province: A distinctive Archaen craton in Laurentian North America, *Can. J. Sci.*, *43*, 1391–1397.
Nolet, G., and F. A. Dahlen (2000), Wavefront healing and the evolution of seismic delay times, *J. Geophys. Res.*, *105*, 19,043–19,054.
Park, J., C. R. Lindberg, and D. J. Thomson (1987), Multiple taper spectral analysis of terrestrial free oscillations: Part 1, *Geophys. J. R. Astron. Soc.*, *91*, 755–794.
Pollitz, F. F. (1999), Regional velocity structure in northern California from inversion of scattered seismic surface waves, *J. Geophys. Res.*, *104*, 15,043–15,072.
Prodehl, C. (1979), Crustal structure of the western United States, *U. S. Geol. Surv. Prof. Pap.*, *1034*, 74 pp.
Rogers, A. M., S. C. Harmsen, E. J. Corbett, K. Priestly, and D. dePolo (1991), The seismicity of Nevada and some adjacent parts of the Great Basin, in *Neotectonics of North America*, edited by D. B. Slemmons et al., vol. 1, pp. 153–184, Geol. Soc. of Am., Boulder, Colo.
Saleeby, J. B. (2003), Segmentation of the Laramide Slab—Evidence from the southern Sierra Nevada, *Geol. Soc. Am. Bull.*, *115*, 655–668.
Saleeby, J. B., and Z. Foster (2004), Topographic response of mantle lithosphere removal in the southern Sierra Nevada region, *Geology*, *32*, 245–248.
Silveira, G., and E. Stutzmann (2002), Anisotropic tomography of the Atlantic Ocean, *Phys. Earth Planet. Inter.*, *132*, 237–248.
Smith, R. B. (1978), Seismicity, crustal structure, and intraplate tectonics of the interior of the western Cordillera, in *Cenozoic Tectonics and Regional Geophysics of the Western Cordillera*, edited by R. B. Smith and G. P. Easton, *Mem. Geol. Soc. Am.*, *152*, 111-144.
Spetzler, J., and R. Snieder (2001), The effect of small-scale heterogeneity on the arrival time of waves, *Geophys. J. Int.*, *145*, 786–796.
Stewart, H. (1988), Tectonics of the Walker Lane Belt, Western Great Basin—Mesozoic and Cenozoic deformation in a zone of shear, in *Metamorphism and Crustal Evolution of the Western United States, Rubey Vol.*, vol. 7, edited by W. Ernst, pp. 684–713, Prentice-Hall, Englewood Cliffs, N. J.
Tape, C., Q. Liu, and J. Tromp (2007), Finite-frequency surface wave tomography using adjoint methods—Methodology and examples using membrane surface waves, *Geophys. J. Int.*, *168*, 1105–1129.
Tikoff, B., and W. McClelland (2005), Transpressional modification of the $^{87}Sr/^{86}Sr$ transition on the western edge of the Idaho batholith, *Geology*, *33*, 469–472.
van der Lee, S., and G. Nolet (1997), Upper mantle S velocity structure of North America, *J. Geophys. Res.*, *102*, 22,815–22,838.
Waite, G. P., R. B. Smith, and R. M. Allen (2006), VP and VS structure of the Yellowstone hot spot from teleseismic tomography: Evidence for an upper mantle plume, *J. Geophys. Res.*, *111*, B04303, doi:10.1029/2005JB003867.
Wielandt, E. (1993), Propagation and structural interpretation of non-plane waves, *Geophys. J. Int.*, *113*, 45–53.
Yang, Y., and D. W. Forsyth (2006), Rayleigh wave phase velocities, small-scale convection, and azimuthal anisotropy beneath southern California, *J. Geophys. Res.*, *111*, B07306, doi:10.1029/2005JB004180.
Yang, Y., and M. H. Ritzwoller (2008), Teleseismic surface wave tomography in the western US using the Transportable Array component of USArray, *Geophys. Res. Lett.*, *35*, L04308, doi:10.1029/2007GL032278.
Zandt, G. (2003), The southern Sierra Nevada drip and the mantle wind direction beneath the southwestern United States, *Int. Geol. Rev.*, *45*, 213–224.
Zhang, X., H. Paulssen, S. Lebedev, and T. Meier (2007), Surface wave tomography of the Gulf of California, *Geophys. Res. Lett.*, *34*, L15305, doi:10.1029/2007GL030631.
Zhao, L., T. H. Jordan, and C. H. Chapman (2000), Three-dimensional Fréchet differential kernels for seismic delay times, *Geophys. J. Int.*, *141*, 558–576.
Zhou, Y., F. A. Dahlen, and G. Nolet (2004), Three-dimensional sensitivity kernels for surface wave observables, *Geophys. J. Int.*, *158*, 142–168.
Zhou, Y., F. A. Dahlen, G. Nolet, and G. Laske (2005), Finite-frequency effects in global surface-wave tomography, *Geophys. J. Int.*, *163*, 1087–1111.

F. F. Pollitz, U.S. Geological Survey, 345 Middlefield Road, MS 977, Menlo Park, CA 94025, USA. (fpollitz@usgs.gov)